Adiabatic Dynamics of Coupled Spins and Phonons in Magnetic Insulators

Shang Ren,[1,2] John Bonini,[2] Massimiliano Stengel,[3,4] Cyrus E. Dreyer,[5,2] and David Vanderbilt[1]

[1]*Department of Physics and Astronomy, Rutgers University, Piscataway, New Jersey 08854, USA*
[2]*Center for Computational Quantum Physics, Flatiron Institute, 162 5th Avenue, New York, New York 10010, USA*
[3]*Institut de Ciència de Materials de Barcelona (ICMAB-CSIC), Campus UAB, 08193 Bellaterra, Spain*
[4]*ICREA-Institució Catalana de Recerca i Estudis Avançats, 08010 Barcelona, Spain*
[5]*Department of Physics and Astronomy, Stony Brook University, Stony Brook, New York 11794-3800, USA*

(Received 10 July 2023; revised 5 December 2023; accepted 2 January 2024; published 7 March 2024)

In conventional *ab initio* methodologies, phonons are calculated by solving equations of motion involving static interatomic force constants and atomic masses. The Born-Oppenheimer approximation, where all electronic degrees of freedom are assumed to adiabatically follow the nuclear dynamics, is also adopted. This approach does not fully account for the effects of broken time-reversal symmetry in systems with magnetic order. Recent attempts to rectify this involve the inclusion of the velocity dependence of the interatomic forces in the equations of motion, which accounts for time-reversal symmetry breaking, and can result in chiral phonon modes with nonzero angular momentum even at the zone center. However, since the energy ranges of phonons and magnons typically overlap, the spins cannot be treated as adiabatically following the lattice degrees of freedom. Instead, phonon and spins must be treated on a similar footing. Focusing on zone-center modes, we propose a method involving Hessian matrices and Berry curvature tensors in terms of both phonon and spin degrees of freedom, and describe a first-principles methodology for calculating these. We then solve Lagrange's equations of motion to determine the energies and characters of the mixed excitations, allowing us to quantify, for example, the energy splittings between chiral pairs of phonons in some cases, and the degree of magnetically induced mixing between infrared and Raman modes in others. The approach is general and can be applied to determine the adiabatic dynamics of any mixed set of slow variables.

DOI: 10.1103/PhysRevX.14.011041

Subject Areas: Computational Physics, Condensed Matter Physics, Magnetism

I. INTRODUCTION

An outstanding challenge of first-principles materials theory is the development of a systematic treatment of the coupled dynamics of phonons and magnons in magnetic materials. The calculation of phonon dispersions has long been a standard feature of modern density-functional theory (DFT) codes based either on finite-difference or linear-response calculations of the dynamical matrix [1–5]. On the other hand, magnon dispersions are most often computed in the context of discrete spin models, sometimes using parameters derived from DFT [6–9], although treatments based on time-dependent DFT (TDDFT) [10–17] and many-body perturbation theory [18–22] have also appeared. However, the consistent treatment of phonon and magnon dynamics on a similar footing, and the coupling between them, remains daunting [23].

Phonons play a crucial role in determining various thermodynamic and electronic properties of materials, including heat capacity, heat transport, electronic conductivity, and superconductivity. Conventionally, phonons are treated within the Born-Oppenheimer approximation [24], i.e., assuming that the electronic degrees of freedom (d.o.f.) can adiabatically follow the motion of the atoms. In these calculations, the potential energy in the phonon Hamiltonian is computed as a function of the atomic displacements. The usual harmonic approximation involves keeping only the leading quadratic dependence of the energy on displacement, encoded in the interatomic force-constant (IFC) matrix, i.e., the Hessian matrix of the energy. Anharmonic treatments go further by taking account of higher-order tensors which describe third and higher derivatives with respect to displacements. These harmonic and anharmonic tensors are all invariant under time-reversal symmetry (TRS), so that at this level of description the phonons are assumed to preserve TRS and possess the symmetries of the nonmagnetic group.

However, this assumption is incorrect for materials with magnetic order or in the presence of an external magnetic field.

Recent efforts have been made to address this issue by incorporating the nuclear Berry potential into the effective Hamiltonian [25–33], which arises naturally when the electronic d.o.f. are integrated out under the Born-Oppenheimer approximation, as first pointed out by Mead and Truhlar [25]. The nuclear Berry potential introduces a velocity-dependent force into the equations of motion (EOM), which is determined by the nuclear Berry curvature multiplied by the nuclear velocity.

Theoretical studies have made several predictions regarding the impact of the nuclear Berry curvature on zone-center chiral phonons [26–29,31–33] and their contribution to the thermal Hall effect [34–37]. Experimental evidence has also emerged supporting the existence of zone-center chiral phonons [38,39] and the phonon thermal Hall effect [40,41]. We define chiral phonons as those that respect rotational symmetry but possess complex eigenvalues under the rotation operator. Chiral phonons have attracted attention due to their unique properties, such as their selective excitation by circular-polarized light with different helicities [38,39,42,43], their coupling to electronic states with distinct chiralities [44] following the selection rule proposed in Ref. [45], and their ability to demonstrate Floquet behavior when driven by lasers [46]. Additionally, chiral phonons can possess phonon magnetic moments [47–49].

To date, much of the theoretical literature treats models in which the nuclear Berry curvature is an adjustable parameter. The first-principles calculation of the nuclear Berry curvature is still in its infancy, with only a few calculations for molecular [30] and crystalline [33] systems.

Spin-wave excitations, or magnons, constitute additional d.o.f. in magnetic materials. These excitations are chiral from the outset; for example, in the presence of easy-axis anisotropy, spins always precess clockwise when viewed endon. While it is not so widely appreciated, magnon dynamics can also be formulated and computed in the context of a geometric-phase framework [50,51]. There is no inertial term in the spin dynamics, but the Berry curvature tensor enters the EOM by describing the spin precession in response to a torque [52]. This raises the possibility of a uniform treatment of both nuclear and spin degrees of freedom in a common theoretical framework.

Crucially, the frequency (or energy) range of the magnons strongly overlaps that of the phonons. In metals these also overlap with electron-hole excitations, but we restrict our attention here to insulators in which there is a clear energy separation between both phonons and magnons on the one hand and cross-gap electronic excitations on the other. In this case, both types of bosonic excitations can be treated as "slow" d.o.f., with the remainder of the electronic system following adiabatically. In such cases, it is crucial to treat both phonon and spin d.o.f. on the same footing.

A first step was taken in this direction in Ref. [33] for the case of bulk ferromagnetic CrI_3. In that work, a minimal model was proposed in which the nuclear Berry curvature arose entirely from the canting of Cr spins in response to atomic displacement. Though this model captured the essential physics of CrI_3, a general and quantitatively accurate theory should include other contributions to the Berry curvature including "phonon-only" Berry curvature arising from atomic displacements at fixed spin, and mixed "spin-phonon" Berry curvature. Such contributions can play an important role, particularly in predicting energy splittings of high-energy chiral phonons. Additionally, Ref. [33] relied on the input of experimental magnon energies, which may not always be available.

Motivated by the need for better fundamental and quantitative understanding of phonons in TRS-broken systems, we present a generalized adiabatic treatment incorporating all relevant Hessian matrices and Berry curvatures for both phonons and spins. It should be noted that the methodology presented in this work provides a general theoretical framework for treating dynamics beyond the specific case of coupled spins and phonons. I.e., it allows for efficient *ab initio* calculation of the adiabatic dynamics of any mixed set of slow variables. This goes significantly beyond the more approximate approach of Ref. [33], which we refer to as the minimal spin-phonon model below. We also demonstrate an *ab initio* methodology to calculate these matrices. We conduct four case studies covering ferromagnetic (FM) and antiferromagnetic (AFM) materials in both three-dimensional (3D) and two-dimensional (2D) form. We investigate the energy splittings and symmetries of chiral phonons in these systems.

We show that, interestingly, circularly polarized chiral phonons do not always exhibit energy splittings when TRS is broken; whether this splitting occurs depends on the point group symmetry in the presence of magnetic order. Also, terms beyond the IFC are needed to correctly capture the symmetry of phonons in cases where magnetic order breaks a spatial symmetry g, but the combination of g and time reversal $\mathcal{T}$ remains a symmetry. This limitation arises because conventional phonon calculations rely on real-symmetric IFC and atomic mass matrices that preserve TRS (if g is a symmetry of the nonmagnetic crystal, but neither g nor $g\mathcal{T}$ remains a symmetry in the presence of magnetic order, the symmetry breaking of g will still manifest itself in the real IFC matrix). We show that correct accounting for phonon symmetries is crucial for determining Raman and infrared (IR) activities.

This paper is organized as follows. In Sec. II, we establish the theoretical framework via the Lagrangian formalism of adiabatic dynamics and derive EOM that treat spins and phonons on an equal footing. We also revisit phonon angular momentum and introduce the concept of atom-resolved phonon angular momentum. Section III details the proposed method for calculating all the matrices

involved in the present approach, along with the computational details. In Sec. IV, we present our results, which include the analysis of phonons and magnons in 3D FM CrI_3 bulk (Sec. IV A), 3D AFM Cr_2O_3 bulk (Sec. IV B), and 2D systems (Sec. IV C) such as FM CrI_3 monolayer (Sec. IV C 1) and AFM $VPSe_3$ monolayer (Sec. IV C 2). Section V provides a discussion of the role of spin-orbit coupling (Sec. V A) and future experimental investigations (Sec. V B). Finally, we summarize our findings and present concluding remarks in Sec. VI.

II. THEORETICAL BACKGROUND

We restrict our considerations to the case of insulating magnetic materials in which there is a clear separation between the energy scales of the phonons and the cross-gap electronic excitations. The magnetic order ensures that there will also be dynamics associated with spin fluctuations, i.e., the magnons. If the magnon frequencies would be higher than, and robustly gapped from, those of the phonons, it would be possible to treat all electronic excitations, including the magnons, as adiabatically following the phonon d.o.f. However, this is almost never the case. In the present work, we therefore treat both the lattice and spin d.o.f. on a similar footing, while assuming that there is still a large energy gap between the top of the phonon or magnon spectrum and the onset of cross-gap electronic excitations.

We formulate our theory in the context of a first-principles mean-field theory such as DFT, where the dynamics of the nuclei is treated classically, while the electronic system is evolved according to the time-dependent Schrödinger equation. This problem is essentially the domain of TDDFT, but here we aim to treat the spin d.o.f. as slow semiclassical variables alongside the nuclear displacements. This requires a separation of the electronic d.o.f. into a small number of spin d.o.f. and the remaining large number of electronic excitations on the scale of the band gap or above.

To do so, we define a "spin" unit vector on a magnetic ion to be the direction of the average spin density inside a Wigner-Seitz sphere centered at that site, and subsequent calculations of electronic ground states and energies are always computed with these spin variables constrained. The essential requirement is that the remaining electronic system, so constrained, should be free of any remaining slow d.o.f., i.e., any below-band-gap excitations. The implementation of the Wigner-Seitz sphere constraint is not a serious obstacle in practice, as most DFT code packages have features for carrying out electronic minimizations under the constraint of fixed spin orientations defined in this way. We emphasize that we treat not only the lattice displacements, but also the spin cantings, in a harmonic approximation about the ground-state reference structure. We treat only collinear easy-axis systems here, and assume that the spin cantings with respect to this axis are small.

To finish a discussion of the approximations of our theory, we note that we use "ordinary" adiabatic dynamics, in which the adiabatic perturbation theory is carried only to first order in the rate of change of nuclear or spin variables. This is well justified as long as the gap separating phonons and magnons from interband electronic excitations is large. And finally, we shortly make a harmonic approximation, in which the atomic displacements and spin cantings are expanded to leading order around a ground-state reference configuration.

With these understandings, we turn now to a detailed presentation of our methodology.

A. Lagrangian formulation of adiabatic dynamics

While the Hamiltonian formalism is commonly used in the literature to analyze chiral phonons [25,26,30,31,33], we will instead start with the Lagrangian formalism. We show in Sec. II C that this approach is well suited to developing a comprehensive model of the coupled spin-phonon dynamics, while avoiding the difficulties associated with defining canonical momentum for spins. The Lagrangian takes the form

$$L = \frac{1}{2}\sum_i M_i \dot{Q}_i^2 - \epsilon(Q) + \hbar \sum_i \dot{Q}_i A_i, \tag{1}$$

where the configuration Q can represent any slow variable. While the formulation is general, we focus on the case that Q represents both the nuclear coordinates and the spin variables, where the latter act as constraints on the spin moments as explained above. For clarity of presentation, we assume a finite number of nuclear and spin d.o.f, as for a molecule or the Γ-point modes of a periodic crystal.

The first term in Eq. (1) is the kinetic energy associated with the ith degree of freedom, where M_i is the nuclear mass for the phonon variables or zero for the spin-canting variables. The second term is the potential energy, and the third represents the coupling between the time derivative of the adiabatic variable Q_i and the Berry potential A_i [50]. The latter is defined as

$$A_i(Q) = \langle \psi(Q) | i \frac{\partial}{\partial Q_i} | \psi(Q) \rangle, \tag{2}$$

where $|\psi(Q)\rangle$ represents the electronic wave function at constrained nuclear coordinates and spin orientations Q.

By solving the Euler-Lagrangian equation for the Lagrangian defined in Eq. (1), we obtain

$$M_i \ddot{Q}_i + \hbar \dot{A}_i = -\partial_i \epsilon(Q) + \hbar \sum_j \dot{Q}_j \partial_i A_j, \tag{3}$$

where ∂_i denotes $\partial/\partial Q_i$. By using $\dot{A}_i = \sum_j \partial_j A_i \dot{Q}_j$, we can simplify Eq. (3) to

$$M_i\ddot{Q}_i = -\partial_i\epsilon(Q) + \hbar\sum_j \dot{Q}_j(\partial_i A_j - \partial_j A_i),$$
$$= -\partial_i\epsilon(Q) + \sum_j G_{ij}(Q)\dot{Q}_j. \quad (4)$$

Here,

$$G_{ij}(Q) = \hbar\Omega_{ij}(Q) = \hbar(\partial_i A_j - \partial_j A_i), \quad (5)$$

where Ω_{ij} is the Berry curvature, and is therefore gauge invariant. Although the gauge-dependent quantity $A_i(Q)$ appears in the Lagrangian, the EOM are gauge invariant since only $G_{ij}(Q)$ appears.

In this work, we focus on small oscillations near equilibrium. To simplify the analysis, we introduce the generalized displacement vector q defined via $Q_i = Q_i^{(0)} + q_i$, where $Q_i^{(0)}$ is the equilibrium value of the ith degree of freedom. Introducing the harmonic approximation, we expand the potential energy $\epsilon(Q)$ in terms of q as

$$\epsilon(Q) = \epsilon(Q_0) + \frac{1}{2}\sum_{ij} K_{ij}q_i q_j + \ldots, \quad (6)$$

where K_{ij} is the Hessian matrix in q_i and q_j, i.e., $K_{ij} = \partial_i\partial_j\epsilon(Q)|_{Q=Q_0}$. The EOM for q is then given by

$$M_i\ddot{q}_i = -\sum_j K_{ij}q_j + \sum_j G_{ij}\dot{q}_j, \quad (7)$$

where $G = G(Q)|_{Q=Q_0}$ is also computed at the reference configuration Q_0. Conventional treatments of phonons in isolation typically use only mass and force-constant matrices M and K, while spin dynamics in isolation is described by the anisotropy tensor K and Berry curvature G. Note that M is real diagonal, K is real symmetric, and G is real antisymmetric.

To determine the frequencies, we substitute $q_i(t) = e^{-i\omega t}q_i$ into Eq. (7), yielding

$$-\omega_n^2 M|q_n\rangle = -K|q_n\rangle - i\omega_n G|q_n\rangle, \quad (8)$$

where $|q_n\rangle$ is a column vector with the ith component $q_{n,i}$ corresponding to the nth mode associated with d.o.f. i. Equation (8) is easily solved using, e.g., the methods of Sec. III C. The above treatment provides a semiclassical theory of the adiabatic dynamics of the system.

B. Mead-Truhlar approach without explicit spin degrees of freedom

If we limit the slow variables Q to include only atomic coordinates, i.e., allowing all electronic degrees of freedom (including spins) to be in their instantaneous ground state for a given Q, we restore the treatment of Mead and Truhlar in Ref. [25]. To indicate the specialization to atomic coordinates, in this section we replace Q and q by R and u, where R denotes the equilibrium position for atomic coordinates, and u denotes the atomic displacement from the equilibrium. Now the EOM for u in the harmonic approximation is

$$M_l^{\mathrm{MT}}\ddot{u}_l = -\sum_m K_{lm}^{\mathrm{MT}}u_m + \sum_m G_{lm}^{\mathrm{MT}}\dot{u}_m, \quad (9)$$

where l and m are composite indices for $I\alpha$, I runs over atoms, and α represents a Cartesian direction. Equation (9) shows that $G_{mn}^{\mathrm{MT}}\dot{u}_n$ corresponds to a force acting on coordinate m that is proportional to the velocity of coordinate n. An alternative derivation of Eq. (9) using the quantum theory in the Hamiltonian framework is given in Appendix A.

The conventional treatment of phonons [1,2] is recovered by discarding the term involving the nuclear Berry curvature G^{MT} in Eq. (9). This is justified in TR-invariant systems, where G^{MT} vanishes by symmetry. However, G^{MT} is often neglected even when the system is not TR symmetric, with the consequences that Eq. (9) obeys TRS and the phonons will not have the correct symmetry of the TRS-broken system. This will force modes with opposite chirality to be degenerate at the zone center, which is not necessarily the case in a magnetic material.

Recent works have used Eq. (9) to demonstrate splitting of chiral modes as a result of TRS breaking [31,33]. However, it was demonstrated in Ref. [33] that for CrI_3, the main contribution to G^{MT} comes from canting and precession of spins. As mentioned earlier, the energy scale for spin rotations corresponds to the frequency of the magnons, which is close to that of the phonons in most systems. Consequently, the assumption that atomic displacements are the only slow d.o.f. in the system, which led to Eq. (9), is not valid. Reference [33] developed a Hamiltonian formalism for coupled spin-phonon dynamics that we refer to here as the "minimal spin-phonon model." In the next section, we develop a more general Lagrangian-based approach that is well suited to treating phonon and spin dynamics together.

C. Treatment of spins and phonons on the same footing

We now return to the framework of Eq. (7) in which q_i includes both nuclear and spin d.o.f. The Euler-Lagrange EOM derived from Eq. (7) is

$$\sum_j M_{ij}\ddot{q}_j = -\sum_j K_{ij}q_j + G_{ij}\dot{q}_j, \quad (10)$$

where i runs over both phonon and spin d.o.f. In the phonon sector, $q_i = u_{I\alpha}$ is a shorthand for a small displacement of atom I in Cartesian direction $\alpha = \{x, y, z\}$. In the spin sector, q_i denotes a small spin canting $q_i = s_{J\beta}$, where J runs only over magnetic ions, and β indexes the spin

canting in the two directions orthogonal to the ground-state spin orientation. Specializing to easy-axis systems with spin axis along $\pm\hat{z}$, we let β run over only the two in-plane Cartesian directions. That is, $q_i = s_{J\beta} = S_{J\beta}/|S_J|$ describes the component $\beta = \{x, y\}$ of the unit vector of spin S_J located on the Jth magnetic ion.

The matrix M_{ij} in Eq. (10) is the diagonal mass matrix introduced in Eq. (1), with zero entries for the spin d.o.f., $K_{ij} = \partial_i\partial_j\epsilon(\mathbf{q})$ is a generalized Hessian matrix, and $G_{ij} = \hbar\Omega_{ij} = \hbar(\partial_i A_j - \partial_j A_i)$ embodies the Berry curvature as in Eq. (5). In these last two expressions, ∂_j denotes $\partial/\partial q_j$, which can be a derivative with respect to either nuclear or spin-canting coordinates evaluated at the reference ground-state configuration. It should be emphasized that in our formulation, the Hessian matrices are expanded to quadratic order in phonon or magnon amplitudes, resulting in a harmonic theory with infinite lifetimes for both phonons and magnons. This is also evident in the hermiticity of Eq. (10). While including anharmonic interactions beyond quadratic order would allow decay of a phonon or magnon excitation into two or more lower-energy excitations, thereby rendering their lifetimes finite, such effects are not considered in this work and remain an area for future investigation.

In this context, derivatives with respect to nuclear coordinates must be taken at fixed spin. That is, the matrices K and G are now computed in terms of the electronic quantum state $|\psi(R, s)\rangle$, rather than $|\psi(R)\rangle$ as in Sec. II B. As explained earlier, this requires a calculation of the electronic ground state subject to constrained spin orientations. While there is some freedom in the definition of the spin unit vector, we follow the established approach of defining it in terms of the integrated spin density inside a Wigner-Seitz sphere, as discussed in Sec. III B. This choice encodes the distinction between "spin" and "other electronic" d.o.f. in our theory.

To simplify the analysis, we can partition all d.o.f. i into phonon d.o.f. (labeled as p) and spin d.o.f. (labeled as s). The matrices in Eq. (10) can then be represented using a block structure as

$$M = \begin{pmatrix} M^{(\mathrm{pp})} & 0 \\ 0 & 0 \end{pmatrix},$$
$$K = \begin{pmatrix} K^{(\mathrm{pp})} & K^{(\mathrm{ps})} \\ K^{(\mathrm{sp})} & K^{(\mathrm{ss})} \end{pmatrix},$$
$$G = \begin{pmatrix} G^{(\mathrm{pp})} & G^{(\mathrm{ps})} \\ G^{(\mathrm{sp})} & G^{(\mathrm{ss})} \end{pmatrix}. \tag{11}$$

We use the term "bare phonons" to refer to phonons that are calculated without considering $G^{(\mathrm{pp})}$, $G^{(\mathrm{ps})}$ ($G^{(\mathrm{sp})}$), or $K^{(\mathrm{ps})}$ ($K^{(\mathrm{sp})}$), while phonons calculated with the inclusion of those terms are referred to as "perturbed phonons." The term "perturbed" is used in recognition of the fact that the influence of these terms is generally small, although we solve Eq. (10) exactly. Nevertheless, we also provide a perturbation analysis of $K^{(\mathrm{sp})}$, $G^{(\mathrm{sp})}$, and $G^{(\mathrm{pp})}$ in Appendix D, illuminating the physical implications of each term, and thereby offering valuable insight.

It is worth noting that $G^{(\mathrm{pp})}$, $G^{(\mathrm{ps})}$ ($G^{(\mathrm{sp})}$), and $K^{(\mathrm{ps})}$ ($K^{(\mathrm{sp})}$) are zero in the absence of spin-orbit coupling (SOC) in collinear systems, a point elaborated upon in Sec. V A below. In that case, the broken TRS in the spin sector is never communicated to the orbital electronic sector or, in turn, to the phonon sector.

Importantly, in the case that $K^{(\mathrm{ps})}$ ($K^{(\mathrm{sp})}$) and $G^{(\mathrm{ps})}$ ($G^{(\mathrm{sp})}$) vanish, phonons and spins decouple, and Eq. (10) reduces to the EOM for phonons and magnons separately. In the phonon sector, it reduces to Eq. (9), which corresponds to the approach proposed by Mead and Truhlar [25]. Meanwhile, in the magnon sector, it reduces to

$$\hbar\Omega^{(\mathrm{ss})}|\dot{s}\rangle = K^{(\mathrm{ss})}|s\rangle, \tag{12}$$

which aligns with the EOM for magnons presented in Ref. [50]. Additionally, when $\Omega^{(\mathrm{ss})}$ is simplified to consider only isolated spinors, rendering interspin elements negligible, Eq. (12) reduces to the well-known Landau-Lifshitz equation [52,53]. Further, if the energies of phonons are considerably lower than those of magnons, Eq. (10) in the phonon sector also reduces to the Mead-Truhlar approach, as discussed in Ref. [33].

The present approach defined by Eqs. (10) and (11) uses Hessian matrices and Berry curvature tensors in terms of all d.o.f. In contrast, the minimal spin-phonon model presented in Ref. [33] included only the spin-spin component of the Berry curvature, so that $G^{(\mathrm{pp})}$, $G^{(\mathrm{ps})}$, and $G^{(\mathrm{sp})}$ were assumed to vanish. Furthermore, the minimal spin-phonon model in Ref. [33] includes only one bare phonon doublet and one bare magnon. In Appendix B, we discuss a more comprehensive version of the spin-phonon model which incorporates all bare phonons and magnons but still neglects $G^{(\mathrm{pp})}$, $G^{(\mathrm{ps})}$, and $G^{(\mathrm{sp})}$, and discuss its connection with the minimal spin-phonon model and its equivalence with the widely employed Landau-Lifshitz equation [52]. We demonstrate that our approach, through the inclusion of nontrivial $\Omega^{(\mathrm{pp})}$, $K^{(\mathrm{sp})}$, and $\Omega^{(\mathrm{sp})}$ terms, provides a fruitful generalization of the Landau-Lifshitz equation.

D. Phonon angular momentum

Before discussing the first-principles methodology to calculate the terms in Eqs. (10) and (11), we review the definition of phonon angular momentum and introduce the concept of atom-resolved phonon angular momentum, as this will be important for characterizing the chiral modes in Sec. IV. The definition of phonon angular momentum can be found in the literature [26], and we briefly revisit the relevant definitions here. First, we note that by solving

Eq. (10), one can obtain an energy eigenvalue ω_n and the corresponding mode with both phonon and spin components, i.e., $|q_n\rangle = |u_n\rangle \oplus |s_n\rangle$, where n runs over different solutions of Eq. (10). Since we are mainly interested in the phonon sector in the present work, we define the atom-resolved phonon angular momentum using the phonon part $|u_n\rangle$ of the mode.

The solutions to the EOM described by Eq. (10) yield energies that differ from those of the bare phonons. However, in all of the systems examined in this work, the differences between these energies and those of the bare phonons are relatively small. As such, we can identify the mode $|q_n\rangle$ as "phononlike" if its energy ω_n is in close proximity to that of a bare phonon. Furthermore, we note that for a phononlike mode $|q_n\rangle$, the $|s_n\rangle$ contributions are very small compared to $|u_n\rangle$. In systems where the frequencies of the phonons and magnons coincide, the aforementioned conditions may not be met; nonetheless, in all cases we consider in this work, the zone-center phonons and magnons of relevance exhibit distinct energies, thus ensuring well-defined phononlike and magnonlike modes.

For phononlike modes, we continue to adopt the normalization convention

$$\langle u_n | M^{(\mathrm{pp})} | u_n \rangle = 1, \tag{13}$$

even though $\langle u_m | M^{(\mathrm{pp})} | u_n \rangle$ is no longer exactly zero for $m \neq n$. It is also possible to have a "perturbed magnon" solution, which is a magnonlike solution with tiny phonon components.

The definition of phonon angular momentum was originally proposed in Ref. [26]. For a phononlike mode $|u_n\rangle$, the atom-resolved phonon angular momentum (ARPAM) $L_{n,Iz}$, for atom I of mass M_I in the z direction is

$$\begin{aligned} L_{n,Iz} &= \hbar M_I \begin{pmatrix} u^*_{n,Ix} & u^*_{n,Iy} \end{pmatrix} \begin{pmatrix} 0 & -i \\ i & 0 \end{pmatrix} \begin{pmatrix} u_{n,Ix} \\ u_{n,Iy} \end{pmatrix} \\ &= 2\hbar M_I \mathrm{Im}[u^*_{n,Ix} u_{n,Iy}], \end{aligned} \tag{14}$$

with $L_{n,Ix}$ and $L_{n,Iy}$ defined similarly by cyclic permutation of Cartesian indices. Note that if the projection of a mode vector on a given atom is of the form $\hat{x} + i\hat{y}$, the atom undergoes a counterclockwise rotation when viewed from above and contributes a positive L_z. The total phonon angular momentum (PAM) [54] $L_{n,z}$ is defined as

$$L_{n,z} = \sum_I L_{n,Iz}, \tag{15}$$

which is the sum of the angular momenta $L_{n,Iz}$ over all atoms I.

The bare phonons solve the secular equation involving only $M^{(\mathrm{pp})}$ and $K^{(\mathrm{pp})}$, which is equivalent to the conventional phonon treatment of Eq. (9) with $G = 0$. These bare phonons can always be chosen real, in which case it follows from Eq. (14) that the full PAM and individual ARPAM always vanish. In the case of degenerate modes, it may be possible to choose chiral linear combinations, but the trace over the degenerate set of modes always results in zero PAM and ARPAM. This is a consequence of the fact that TRS has not yet been broken at the bare level of description.

III. METHODS

A. Finite-difference method

This section demonstrates how to compute all matrices in Eq. (11) using finite-difference methods in the context of first-principles calculations. The nuclear masses $M^{(\mathrm{pp})}$ are trivially known. All calculations are carried out using the DFT methodology described in Sec. III B at fixed atomic coordinates and fixed spin orientations, where the latter are defined in terms of an integration of the spin density over a Wigner-Seitz sphere as mentioned earlier.

The force-constant matrix $K^{(\mathrm{pp})}$, which is also the Hessian matrix of the energy with respect to nuclear d.o.f., is defined as

$$K^{(\mathrm{pp})}_{lm} = \frac{\partial^2 \epsilon}{\partial u_l \partial u_m} = -\frac{\partial F_l}{\partial u_m}. \tag{16}$$

Here, l and m run over nuclear d.o.f., and ϵ is the total energy $\epsilon(s, R)$ of the configuration s, R. The matrix element $K^{(\mathrm{pp})}_{lm}$ is computed by taking the finite difference of the Hellmann-Feynman forces F_l [1,2] while constraining the spin directions to lie along $\hat{z}$.

The Hessian matrix of the energy with respect to spin d.o.f. is denoted by $K^{(\mathrm{ss})}$, with elements defined as

$$K^{(\mathrm{ss})}_{ab} = \frac{\partial^2 \epsilon}{\partial s_a \partial s_b}, \tag{17}$$

where a and b run over spin d.o.f. To calculate $K^{(\mathrm{ss})}$, we compute the second derivatives of the total energy with respect to small canting of the spins. Specifically, letting $s_a = s_{I\alpha}$ and $s_b = s_{J\beta}$, for each pair (I, J) we compute the energies of $(\alpha, \beta) = \pm(0.02, 0)$, $\pm(0, 0.02)$, and $\pm(0.02, 0.02)$ relative to the ground state, while constraining all other spin moments to remain along $\hat{z}$.

The spin-phonon Hessian matrix $K^{(\mathrm{sp})}$ is defined as

$$K^{(\mathrm{sp})}_{al} = \frac{\partial^2 \epsilon}{\partial s_a \partial u_l} = -\frac{\partial F_l}{\partial s_a}, \tag{18}$$

where a and l, respectively, run over the spin and nuclear d.o.f. $K^{(\mathrm{sp})}_{al}$ is computed by taking the finite-difference derivative of the force F_l with respect to the spin coordinate s_a.

An alternative approach to calculating $K^{(\mathrm{sp})}$ was described in Ref. [33]. Near the ground state, the energy ϵ of the entire system can be expanded as

$$\epsilon = \frac{1}{2}\sum_{lm} K^{(\mathrm{pp})}_{lm} u_l u_m + \sum_{al} K^{(\mathrm{sp})}_{al} s_a u_l + \frac{1}{2}\sum_{ab} K^{(\mathrm{ss})}_{ab} s_a s_b. \quad (19)$$

As ϵ is minimized with s_a, we have

$$\frac{\partial \epsilon}{\partial s_a} = \sum_{l} K^{(\mathrm{sp})}_{al} u_l + \sum_{b} K^{(\mathrm{ss})}_{ab} s_b = 0. \quad (20)$$

We define a spin response matrix $\chi^{(\mathrm{sp})}$ as

$$\chi^{(\mathrm{sp})}_{al} = \frac{\partial s_a}{\partial u_l} \simeq \frac{s_a}{u_l}, \quad (21)$$

where the second equality holds if both s_a and u_l are small. Then we can obtain

$$K^{(\mathrm{sp})} = -K^{(\mathrm{ss})}\chi^{(\mathrm{sp})}, \quad (22)$$

where we restore the matrix form for simplicity. In practice, one can perturb the ground-state structure with u_l by manually moving the atoms from the equilibrium position and calculate the spin canting s_a with respect to u_l. We use Eq. (22) to calculate $K^{(\mathrm{sp})}$ for bulk CrI_3, and the result is consistent with Eq. (18). However, due to the slow convergence of spin relaxation, we recommend using Eq. (18) to calculate $K^{(\mathrm{sp})}$.

In Eq. (11), G is simply $\hbar$ times Ω, where Ω is the Berry curvature. The latter is computed using Stokes's theorem as expressed by

$$\Omega_{ij} = \frac{\Phi_{ij}}{2|\delta q_i \wedge \delta q_j|}, \quad (23)$$

where i and j run over all d.o.f., and Φ_{ij} is the Berry phase around a diamond-shaped region of parameter space whose area appears in the denominator. Specifically, e.g., for a finite system with electronic ground-state wave function $|\psi\rangle$,

$$\Phi_{ij} = -\mathrm{Im}\ \ln[\langle\psi(+\delta q_i)|\psi(+\delta q_j)\rangle\langle\psi(+\delta q_j)|\psi(-\delta q_i)\rangle \times \langle\psi(-\delta q_i)|\psi(-\delta q_j)\rangle\langle\psi(-\delta q_j)|\psi(+\delta q_i)\rangle]. \quad (24)$$

In an extended crystal with a single occupied band, one must sum over the Bloch wave vector k in the Brillouin zone to obtain $\Phi_{ij} = N_k^{-1}\sum_k \Phi^{(k)}_{ij}$, where $\Phi^{(k)}_{ij}$ is defined as in Eq. (24) but with ψ replaced by the Bloch function ψ_k. Φ_{ij} now has the interpretation of a Berry phase per unit cell, consistent with the interpretation of the Hessian K as an energy per unit cell. To extend $\Phi^{(k)}_{ij}$ to the multiband case, we can replace the inner product of two Bloch states with the overlap matrix in the usual way [55] as

$$\Phi^{(k)}_{ij} = -\mathrm{Im}\ \ln\ \det[M^k(+\delta q_i, +\delta q_j)M^k(+\delta q_j, -\delta q_i) \times M^k(-\delta q_i, -\delta q_j)M^k(-\delta q_j, +\delta q_i)]. \quad (25)$$

Here, the overlap matrices are defined as

$$M^k_{mn}(\delta q_i, \delta q_j) = \langle\psi_{mk}(\delta q_i)|\psi_{nk}(\delta q_j)\rangle, \quad (26)$$

where m and n are band indices. When computing the matrices, a finite difference of 0.015 Å is used for the phonon d.o.f., and 0.02 is used for the spin d.o.f. We take care to choose these finite differences to ensure they remain within the linear regime. The numerical values of $K^{(\mathrm{ss})}$ and $G^{(\mathrm{ss})}$ for all four studied materials can be found in Appendix C.

B. First-principles calculations

In this section, we provide computational details for calculating matrices using the finite-difference method described in Sec. III A. The reported DFT calculations are performed using the Vienna *ab initio* simulation package [56–58], employing the local-density-approximation (LDA) exchange-correlation functional [59] and the projector-augmented-wave [60] method, with Cr $3s^2 3p^6 3d^5 4s^1$, I $5s^2 5p^5$, O $2s^2 2p^4$, V $3s^2 3p^6 3d^5$, P $3s^2 3p^3$, Se $4s^2 4p^4$ pseudo potential valence configurations. A plane-wave cutoff of 520 eV is adopted for the CrI_3 calculations, and 500 eV for the Cr_2O_3 and $VPSe_3$ systems.

All structures are relaxed using the local spin-density approximation, and the convergence criteria for forces and energies are 10^{-3} eV/Å and 10^{-8} eV, respectively. After relaxation, the wave functions are calculated using static calculations with a convergence criterion of 10^{-10} eV for energies. Spin-orbit coupling, which is essential to the physics described in this work, is included in all static calculations except structural relaxations.

We use Γ-centered Monkhorst-Pack k-points meshes [61] for all calculations, specifically $5\times5\times5$ and $7\times7\times7$ for bulk CrI_3 and Cr_2O_3, respectively, and $7\times7\times1$ and $6\times6\times1$ for monolayer CrI_3 and $VPSe_3$, respectively. For Cr_2O_3 and $VPSe_3$, the Dudarev-type DFT + U approach [62] is used, with values of $U = 4.0$ eV and $J = 0.6$ eV for Cr and $U = 3.25$ eV, and $J = 0$ for V (adapted from Refs. [63,64]). For constrained local-moment calculations, the Wigner-Seitz radii for Cr and V are 1.164 and 1.217 Å, respectively. The overlap matrix [Eq. (26)] is calculated as in Ref. [65]. Symmetry analysis is performed using the FINDSYM [66] and SPGLIB [67] packages, while figures are rendered using VESTA [68].

C. Solution of the equations of motion

In this section, we introduce a practical method for solving the EOM in Eq. (10). Given that the generalized mass matrix is noninvertible, conventional approaches are

not directly applicable. We proceed as follows, although other potential methods may be suitable.

First, we rewrite Eq. (10) as

$$\frac{d}{dt}\begin{pmatrix} u \\ \dot{u} \\ s \end{pmatrix} = \begin{pmatrix} 0 & 1 & 0 \\ A_1 & A_2 & A_3 \\ B_1 & B_2 & B_3 \end{pmatrix}\begin{pmatrix} u \\ \dot{u} \\ s \end{pmatrix}, \tag{27}$$

which can be shown to reduce to Eq. (10) with the definitions

$$\begin{aligned} A_1 &= -[M^{(\mathrm{pp})}]^{-1}K^{(\mathrm{pp})} + [M^{(\mathrm{pp})}]^{-1}G^{(\mathrm{ps})}[G^{(\mathrm{ss})}]^{-1}K^{(\mathrm{sp})}, \\ A_2 &= [M^{(\mathrm{pp})}]^{-1}G^{(\mathrm{pp})} - [M^{(\mathrm{pp})}]^{-1}G^{(\mathrm{ps})}[G^{(\mathrm{ss})}]^{-1}G^{(\mathrm{sp})}, \\ A_3 &= -[M^{(\mathrm{pp})}]^{-1}K^{(\mathrm{ps})} + [M^{(\mathrm{pp})}]^{-1}G^{(\mathrm{ps})}[G^{(\mathrm{ss})}]^{-1}K^{(\mathrm{ss})}, \\ B_1 &= [G^{(\mathrm{ss})}]^{-1}K^{(\mathrm{sp})}, \\ B_2 &= -[G^{(\mathrm{ss})}]^{-1}G^{(\mathrm{sp})}, \\ B_3 &= [G^{(\mathrm{ss})}]^{-1}K^{(\mathrm{ss})}. \end{aligned} \tag{28}$$

The eigenvalues (multiplied by i) of the matrix in Eq. (27), denoted as ω_n, correspond to the solutions of Eq. (10). We restrict the index n to run over only solutions for which $\omega_n > 0$, which we take to be the physically meaningful ones.

In practice, we find that small numerical errors remain in the eigenvectors, which arise from the fact that a Hermitian eigensolver cannot be applied in the context of Eq. (27). We find that these errors can easily be removed by following with a second step in which we substitute the computed energies ω_n back into Eq. (10) and then apply a Hermitian eigensolver to recalculate the eigenvectors.

IV. RESULTS

We conduct four case studies covering both FM and AFM systems, in both 3D and 2D. In Sec. IV A, we present the results obtained from our present approach for bulk CrI_3, focusing on chiral phonons. The significance of the Berry curvatures neglected in Ref. [33], is discussed in Sec. IV A 1, while the relevant solutions for the magnons are discussed in Sec. IV A 2. Subsequently, in Sec. IV B, we investigate the phonons and magnons in bulk Cr_2O_3 using the present approach. Shifting our focus to monolayer systems in Sec. IV C, we first consider 2D FM CrI_3 in Sec. IV C 1, and then 2D AFM $VPSe_3$ in Sec. IV C 2.

A. Chiral phonons in bulk ferromagnetic CrI_3

CrI_3 is a hexagonal van der Waals material that exhibits FM order in both bulk and monolayer phases [69]. It is an insulator with inversion and threefold-rotational symmetry around the z axis in both phases. The magnetic moments on the Cr ions do not break the inversion symmetry. The symmetries are discussed in detail below.

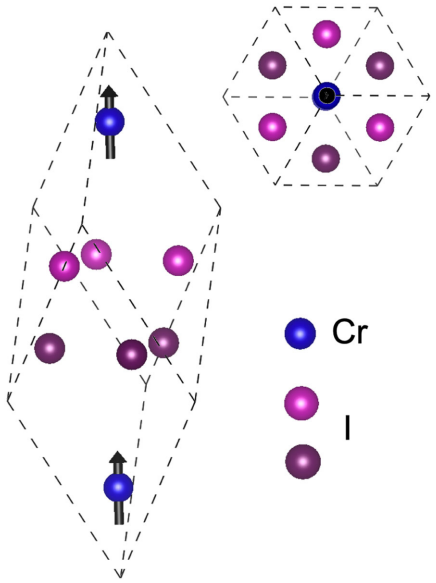

FIG. 1. Visualization of crystal structure and magnetic moments of a bulk CrI_3 unit cell. Cr atoms are depicted in blue, while top-layer and bottom-layer I atoms are in bright and dark magenta, respectively. The black vectors indicate the magnetic moments, which are oriented along the z direction.

The crystal structure of the bulk CrI_3 unit cell is depicted in Fig. 1. For bulk CrI_3, the structural and magnetic symmetries are identical (space group $R\bar{3}$, point group S_6), regardless of the presence of FM order. That is, the magnetic space group is of type I ("colorless"), in which no symmetry operations involve TR [70]. Therefore, the zone-center phonons can be categorized into the irreducible representations (irreps) of the S_6 point group as $4E_g \oplus 4E_u \oplus 4A_g \oplus 4A_u$. Among these, one A_u mode and one pair of E_u modes are acoustic modes. In this work, we focus on the optical modes.

The E_g and E_u irreps are complex-conjugate irreps, which are more properly decomposed further into one-dimensional irreps of opposite chirality. In the presence of TRS, or when neglecting the term involving the Berry curvature G tensor in Eq. (9), the two modes making up one of these E irreps are degenerate. However, this degeneracy is broken by the FM order, which induces a nonzero Berry curvature via the SOC as discussed Sec. II.

We first present our results for the case of the E_g and E_u phonons in Table I. The energy shifts ΔE represent the differences between the bare phonon frequencies E_0 computed using only the force-constant term $K^{(\mathrm{pp})}$ in Eq. (9), and the modified energy obtained from the present approach of Eq. (10) or from the spin-phonon model of Appendix B [71]. The PAM L_z of each phonon is also reported for the present approach.

From Table I, we observe that all E_g and E_u bare phonons are doubly degenerate, while the degeneracy is broken for the perturbed phonons. Although our numerical solution for the bare modes initially yields a pair of real phonons $|u_1\rangle$ and

TABLE I. Computed properties of zone-center E_g and E_u phonons in bulk CrI_3. Energy shifts ΔE are defined relative to the bare phonon energies E_0, and are shown for both the present approach and the spin-phonon model. $\chi(C_3)$ is the C_3 eigenvalue indicating the chirality of the mode ($\varepsilon = e^{2\pi i/3}$), and L_z is the phonon angular momentum of Eq. (15).

	Bare	Present approach		Spin phonon	
Irrep	E_0 (meV)	ΔE (meV)	$L_z(\hbar)$	ΔE (meV)	$\chi(C_3)$
E_g	7.0000	−0.0017	0.1259	−0.0013	ε^*
		0.0022	−0.1264	0.0016	ε
	12.9288	−0.0007	−0.1325	−0.0005	ε^*
		0.0007	0.1351	0.0006	ε
	13.4876	−0.0007	0.1740	−0.0002	ε^*
		0.0007	−0.1761	0.0003	ε
	29.8518	−0.0028	0.8325	-1.26×10^{-6}	ε^*
		0.0028	−0.8326	1.31×10^{-6}	ε
E_u	10.7687	−0.0052	0.2352	−0.0045	ε
		−0.0009	−0.2344	−0.0016	ε^*
	14.3295	−0.0170	0.7173	−0.0175	ε
		−0.0042	−0.7192	−0.0040	ε^*
	27.8225	0.0037	0.9537	−0.0035	ε^*
		0.0272	−0.9545	0.0356	ε

$|u_2\rangle$, we resolve these into eigenstates of the C_3 symmetry operator. We first ensure that $\langle u_2|C_3|u_1\rangle$ is positive, flipping the sign of $|u_2\rangle$ if not, and then construct the bare chiral modes $|u_\pm\rangle = (|u_1\rangle \mp i|u_2\rangle)/\sqrt{2}$ belonging to eigenvalues $\varepsilon = \exp(i2\pi/3)$ and $\varepsilon^* = \exp(-i2\pi/3)$, respectively. We designate these as "+" and "−" modes, and refer to them as belonging to the ε and ε^* symmetry sectors, respectively. The former (latter) are characterized by a clockwise (counterclockwise) rotation of the Cr atoms when viewed from above.

The numerical solutions for the perturbed phonons automatically generate chiral C_3 eigenstates, and we find that each of these solutions is almost identical to the bare chiral mode of the same symmetry that is closest in energy. There is only a small admixture of other bare modes belonging to the same sector. This allows a straightforward association of bare and perturbed modes as shown in Table I.

Table I demonstrates that the E_u phonons with ε chirality have the largest energy corrections. This follows from their close energy proximity to the E_u magnons, which also possess ε chirality. A detailed discussion of magnons in bulk CrI_3 is provided in Sec. IV A 2, and a perturbative treatment of phonon-magnon interactions is presented in Appendix D. The pronounced effect on the E_u phonons is further evident in Eq. (D20), where the phonons with ε chirality have the smallest energy denominators.

We briefly address the expected uncertainties in our first-principles calculations of the $K^{(\mathrm{sp})}$, $G^{(\mathrm{sp})}$, and $G^{(\mathrm{pp})}$ matrices, as these are the matrices that contribute to the energy shifts (see Appendix D). First, we analyze the fitting errors for $K^{(\mathrm{sp})}$ associated with our finite-difference methodology, which is done via linear regression of the forces against spin-canting angles. We find that the norm of the fitting error is roughly 1.5% of the norm of $K^{(\mathrm{sp})}$ itself. A second useful metric is the norm of the residual resulting from symmetrization of a matrix relative to the norm of the matrix itself, which we find to be 0.4%, 2.0%, and 2.7% for $K^{(\mathrm{sp})}$, $G^{(\mathrm{sp})}$, and $G^{(\mathrm{pp})}$, respectively. The perturbation analysis of Eqs. (D20) and (D32) indicates that the energy shifts and splittings are quadratic in $K^{(\mathrm{sp})}$ and $G^{(\mathrm{sp})}$ and linear in $G^{(\mathrm{pp})}$. This implies overall errors on the order of 3%–4% in the values reported above for these shifts and splittings.

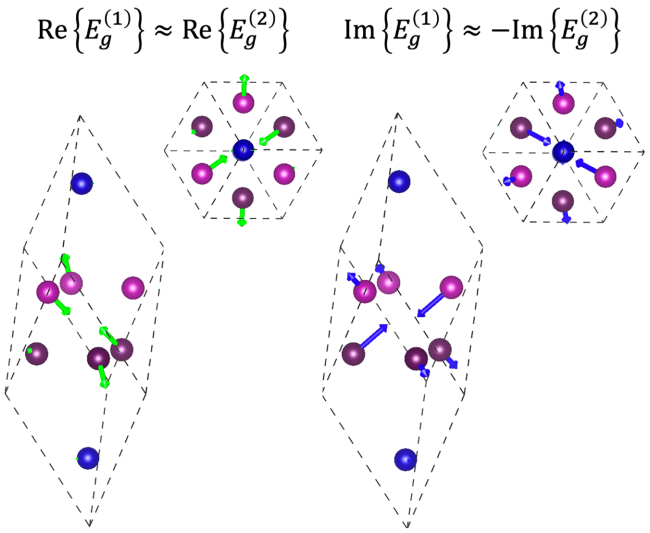

FIG. 2. Visualization of the real and imaginary components of the chiral phonons $E_g^{(1)}$ and $E_g^{(2)}$. Cr atoms are depicted in blue, while top-layer and bottom-layer I atoms are in bright and dark magenta, respectively. The green vectors represent the real part of the phonon displacement, and the blue vectors represent the imaginary part. The real part of $E_g^{(1)}$ and $E_g^{(2)}$ are nearly identical, while the imaginary parts are in opposite directions.

In Fig. 2, we visualize the real and imaginary parts of two E_g chiral phonons around 7 meV, denoted as $E_g^{(1)}$ for the mode with lower energy and $E_g^{(2)}$ for the mode with higher energy. It is apparent that those two chiral phonons are approximately complex conjugates of each other.

Note that the argument about energy splitting based on point group irreps can be generalized to any magnetic material with a point group that includes an E-type irrep (E, E_g, or E_u) consisting of two 1D irreps when complex representations are allowed, indicating that similar phonon energy splittings can be expected in such materials.

The phonon angular momentum is calculated using Eqs. (14) and (15), and the results are listed in Table I. Because of the C_3 symmetry, the total angular momentum of a given chiral phonon can have only a z component. We find values of $|L_z|$ ranging from 0.13 to 0.95 in units of $\hbar$, indicative of a substantial angular momentum for many of the chiral phonons, especially the higher-frequency ones.

We find that the bare circular modes constructed as $|u_\pm\rangle = (|u_1\rangle \mp i|u_2\rangle)/\sqrt{2}$ from the real bare modes can be used to evaluate the PAM to a good approximation. The results are close to those shown in Table I, with a typical error of $10^{-3}\hbar$ in $|L_z|$. However, when calculating the PAM in this way, the angular momentum vanishes exactly when summed over any pair of chiral phonons, which have equal and opposite L_z values. In contrast, solutions using the full matrices of Eq. (10) reveal that the cancellation is no longer perfect, and the total angular momentum of a pair is small but nonzero. The slight discrepancy between the two $|L_z|$ values arises from the magnon-mediated phonon-phonon mixing, which appears at second order in the phonon-magnon coupling and therefore makes only a minor contribution. We provide a more detailed discussion on this topic based on a perturbation approach in Appendix D 1.

1. Importance of $G^{(\mathrm{pp})}$ and $G^{(\mathrm{ps})}$ in calculating energies

The methodology of Ref. [33] for CrI_3 differs from the approach of this work [i.e., Eqs. (10) and (11)] in the following ways. First, the only Berry curvature considered in Ref. [33] was $G^{(\mathrm{ss})}$. Second, the minimal model in Ref. [33] only considers the interaction between one magnon and each phonon doublet separately, neglecting the mixing between bare phonon doublets. In Appendix B, we discuss a more comprehensive version of that model which still neglects $G^{(\mathrm{pp})}$, $G^{(\mathrm{sp})}$, and $G^{(\mathrm{ps})}$ but incorporates all bare phonons and magnons. To show the importance of $G^{(\mathrm{pp})}$ and $G^{(\mathrm{sp})}$ ($G^{(\mathrm{ps})}$) in accurately determining energy splittings, we also apply the model present in Appendix B to calculate chiral phonon energies for the E_g and E_u modes, and the results are presented in Table I.

As shown in Table I, both methods exhibit an energy splitting of chiral modes compared to bare phonons. The energy splitting of low-energy E_g and E_u phonons is similar to that obtained using the present approach, suggesting that $G^{(\mathrm{pp})}$ and $G^{(\mathrm{ps})}$ have little effect on those modes. However, for high-energy E_g and E_u phonons, the spin-phonon model results differ significantly, indicating the importance of $G^{(\mathrm{pp})}$ and $G^{(\mathrm{ps})}$ for these phonons. Specifically, the absolute values of the $G^{(\mathrm{pp})}$ matrix elements for these four E_g modes are $\{0.995, 0.254, 0.972, 5.623\}$ in units of μeV. The highest-energy E_g modes exhibit substantially greater values, leading to a pronounced energy splitting. Appendix D 3 details the perturbative analysis of $G^{(\mathrm{pp})}$, with Eq. (D32) specifying the energy corrections attributed to the $G^{(\mathrm{pp})}$ term. As indicated by Eq. (D32), $G^{(\mathrm{pp})}$ primarily accounts for the substantial splitting observed in the highest-energy E_g mode, with both direct computation and perturbative treatment yielding a correction of ± 0.0028 meV.

Interestingly, we find that the PAM calculated using the spin-phonon model (not shown) is in good agreement with the present approach with an error of the order of $10^{-4}\hbar$, suggesting that the phonon vectors are not very different regardless of whether $G^{(\mathrm{pp})}$ and $G^{(\mathrm{ps})}$ are included or not.

TABLE II. Computed properties of zone-center A_g and A_u phonons in bulk CrI_3. Energy shifts ΔE are defined relative to the bare phonon energies E_0. L_z is the phonon angular momentum of Eq. (15).

Irrep	E_0 (meV)	ΔE (10^{-8} meV)	$L_z(10^{-4}\hbar)$
A_g	9.95	−8.8	1.99
	11.35	2.6	−2.37
	16.50	−50.6	−1.07
	26.51	98.6	1.96
A_u	8.13	−4.5	−1.16
	16.60	−7.9	2.65
	31.74	32.7	−0.52

We now turn to a consideration of the A_g and A_u modes. The spin-phonon model presented in Appendix B has no effect on the A_g and A_u phonons, since $K^{(\mathrm{sp})}$ gives the coupling to magnons, and there are no zone-center magnons in these symmetry sectors. Considering the present approach, although all (ss) and (sp) terms are absent in the A_g and A_u sectors, the $G^{(\mathrm{pp})}$ matrix does not vanish and causes a slight mixing between two different A_g (or A_u) bare phonons. That is, we can write $|u_n\rangle \simeq |u_n^{(0)}\rangle + i\sum_m \delta_m |u_m^{(0)}\rangle$, where $|u_{\{n,m\}}^{(0)}\rangle$ represents the bare phonons from A_g (or A_u) irrep. Here, $i\delta_m$ is purely imaginary and expected to be small, attributed to the minor size of the $G^{(\mathrm{pp})}$ matrix element, as discussed in Appendix D 3.

This mixing results in a nonzero PAM and nonzero energy shift of each phonon relative to its bare energy. Although these phonons exhibit nonzero PAM, we refrain from referring to them as "chiral phonons" because they belong to the $\chi(C_3) = 1$ sector of modes that are invariant under the C_3 operation. Instead, we refer to them as $(1 + i\delta)$-type perturbed phonons, or simply perturbed phonons.

The energy shifts and PAM for A_g and A_u perturbed phonons are presented in Table II, and the real and imaginary parts of the A_g perturbed phonon near 10 meV ($A_g^{(1)}$) are visualized in Fig. 3.

2. Bare and perturbed magnons

So far, we focused solely on the phononlike solutions of the equation of motion given by Eq. (10) in the present approach [or Eq. (B1) for the spin-phonon model]. Nevertheless, these equations also admit magnonlike solutions, which we call "perturbed magnons." In this section, we investigate the impact of phonons on the magnon spectrum, using bulk CrI_3 as a case study. The numerical values for the matrices $K^{(\mathrm{ss})}$ and $G^{(\mathrm{ss})}$ are provided in Appendix C.

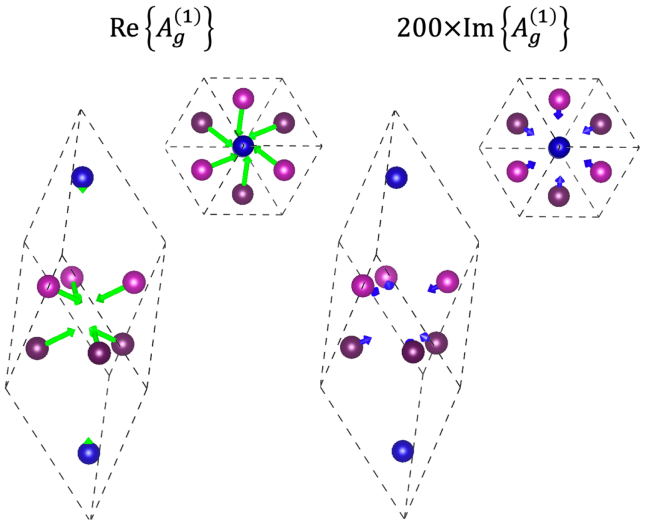

FIG. 3. Visualization of the real and imaginary components of the perturbed phonon $A_g^{(1)}$. Cr atoms are depicted in blue, while top-layer and bottom-layer I atoms are in bright and dark magenta, respectively. The green vectors represent the real part of the phonon displacement, and the blue vectors represent the imaginary part, which are amplified 200 times.

The EOM for a bare magnon without any phonon-magnon interaction is given by Eq. (12). The energies of bare magnons are listed in Table III. The E_g magnon corresponds to the acoustic mode, where the two Cr spins have the same canting, while the E_u magnon corresponds to the optical mode, where the two Cr spins have opposite canting. Both magnons have positive energies and belong to the + sector with $\chi(C_3) = \varepsilon$, indicating that the two Cr spins are rotating clockwise [72].

The perturbed magnons have slightly modified energies (Table III). The energy change from the bare magnon for the E_u mode is more significant compared to the E_g magnon, since the E_u phonons are closer to the E_u magnon in the energy spectrum. By far the most significant contribution to the energy shifts is the inclusion of $K^{(\mathrm{sp})}$; neglecting the $G^{(\mathrm{pp})}$, $G^{(\mathrm{sp})}$, and $G^{(\mathrm{ps})}$ terms changes the energies by less than 0.4 μeV. A perturbation treatment of magnon energies is provided in Appendix D 1.

Note that the equations of motion have two additional negative-energy magnon solutions belonging to the − sector with $\chi(C_3) = \varepsilon^*$. These correspond to the counterclockwise precession of spins and are not physically observable. Nonetheless, they still influence the system dynamics through their interaction with physical − phonons, which acquire some magnon dressing in which the spin vectors are forced to precess in the unnatural counterclockwise sense. This influence of negative-energy magnons becomes clear from the perturbation analysis presented in Appendix D, where the summation index μ in Eq. (D16) and Eqs. (D19) and (D20) runs over all solutions of Eq. (D3), including those of negative energy. However, since the energy denominators in Eq. (D20) are larger when coupling to negative-energy solutions, the magnon dressing is typically smaller. This explains why the + phonons, which couple to positive-energy magnon solutions, are more strongly perturbed than the − ones, which do not. This can be seen in Table I, where it is especially noticeable for the E_u modes.

TABLE III. Energies of the bare magnons E_0, energy shifts of perturbed magnon modes compared to bare magnons ΔE, and the corresponding C_3 eigenvalues $\chi(C_3)$ for both E_g and E_u modes in bulk CrI_3.

Irrep	E_0 (meV)	ΔE (meV)	$\chi(C_3)$
E_g	0.5902	−0.0046	ε
E_u	22.8635	−0.0224	ε

B. Phonons in antiferromagnetic Cr_2O_3

In this section, we present our results for the phonons in bulk Cr_2O_3. As shown in Fig. 4, Cr_2O_3 has an AFM insulating ground state with antiparallel magnetic moments aligned along the threefold-rotational z axis.

The magnetic symmetry of Cr_2O_3 is richer than that of CrI_3, in that it belongs to a type III ("black-white") magnetic group [70]. Since we are interested in zone-center phonons, we frame our discussion in terms of the magnetic point group $\mathcal{G}$. The black-white character means that half the elements of $\mathcal{G}$ come with the TR operator $\mathcal{T}$ and half come without. The latter half form a "unitary subgroup" $\mathcal{H}$, and the

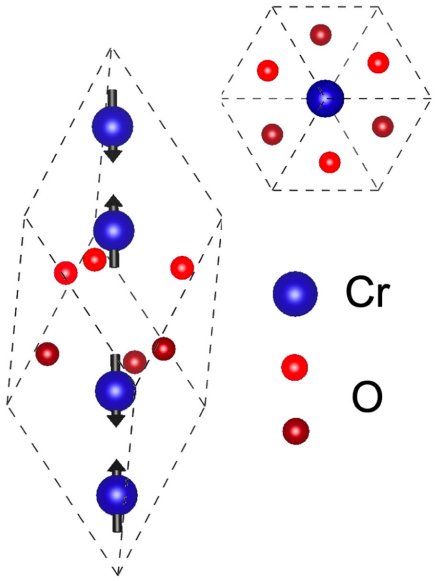

FIG. 4. A visualization of the crystal structure and magnetic moments of the unit cell of bulk Cr_2O_3. The Cr atoms are depicted in blue, while the top-layer and bottom-layer O atoms are shown in bright and dark red, respectively. The black vectors indicate the magnetic moments, which are oriented along the z direction.

others are of the form $g\mathcal{H}$ where g is one of the antiunitary operators in $\mathcal{G}$. The "structural point group" $\bar{\mathcal{G}}$ contains the same list of operators as in $\mathcal{G}$, except that $\mathcal{T}$ is removed from all the antiunitary operators. The important point in what follows is that while the Hessian matrices are even under all elements of $\bar{\mathcal{G}}$, the Berry curvature matrices are even under the elements of $\mathcal{H}$ and odd under the elements of $\bar{\mathcal{G}} - \mathcal{H}$. As a consequence, when the Berry curvature is included, the irreps of unitary subgroup $\mathcal{H}$, not the structural group $\bar{\mathcal{G}}$, should be used to label the perturbed modes of this system.

In the case of Cr_2O_3, the magnetic space group is $R\bar{3}'c'$, and the structural point group is D_{3d}. The magnetic ordering on the Cr sublattice breaks inversion (i), dihedral mirror (σ_d), and rotoinversion (S_6) symmetries, reducing the unitary point group to D_3, whose irreps will be used to label our perturbed phonons and magnons. The corresponding time-reversed operators $i\mathcal{T}$, $\sigma_d\mathcal{T}$, and $S_6\mathcal{T}$ are present in the magnetic point group, but being antiunitary, they do not induce any additional irreps.

While the experimental magnetic moment of Cr_2O_3 is found to be along the z direction, DFT calculations predict an in-plane magnetic moment. This discrepancy can be resolved by applying a 2% epitaxial strain, which results in an easy-axis ground state [63]. To ensure consistency with the experimental ground state, we apply a 2% epitaxial strain in our calculations, as our approach assumes spins to be oriented along the z direction.

As previously discussed, the irreps of point group D_3 should be used to characterize zone-center perturbed phonons, which can be decomposed into $4A_1 \oplus 6A_2 \oplus 10E$. Among them, one A_2 and two E modes correspond to acoustic phonons. According to the character table of D_3, the E irreps have to be 2D irreps, indicating that there is no degeneracy breaking or energy splitting compared to bare phonons. This is confirmed by the numerical results of perturbed phonon energies, which are presented in Table IV. It is worth noting that the perturbed phonon energies differ from those of the bare phonons, which are also included in Table IV for reference purposes.

1. Mixing of phonon irreps

As mentioned earlier, although i, σ_d, and S_6 are no longer symmetries, $i\mathcal{T}$, $\sigma_d\mathcal{T}$, and $S_6\mathcal{T}$ remain symmetries of the system. On the other hand, the matrices $K^{(\mathrm{pp})}$ and $M^{(\mathrm{pp})}$ are both real. Applying the symmetry operations $i\mathcal{T}$, $\sigma_d\mathcal{T}$, and $S_6\mathcal{T}$ to these matrices is equivalent to applying i, σ_d, and S_6, respectively. Therefore, $K^{(\mathrm{pp})}$ and $M^{(\mathrm{pp})}$ are symmetric not only under the D_3 symmetry operations, but also under i, σ_d, and S_6, resulting in a point group symmetry of D_{3d}.

This higher symmetry of $K^{(\mathrm{pp})}$ and $M^{(\mathrm{pp})}$ has an important impact on the symmetries of zone-center bare phonons, which are calculated using $K^{(\mathrm{pp})}$ and $M^{(\mathrm{pp})}$: Bare phonons at the Γ point must have D_{3d} symmetry, and thus can be labeled by the irreps of D_{3d}. The Γ point bare phonons decompose into $5E_g \oplus 5E_u \oplus 2A_{1g} \oplus 2A_{1u} \oplus 3A_{2g} \oplus 3A_{2u}$, where one E_u doublet and one A_{2u} mode are acoustic modes. The irreps of the bare phonons are included in Table IV.

TABLE IV. Bare phonon irreps, energies, ARPAM of Cr atoms in the z direction (Cr L_z), ARPAM of O atoms in the x direction (O L_x), and interirrep mixing (ρ) of perturbed phonons in bulk Cr_2O_3. The bare phonon energies E_0 are included as a reference for the energy shifts ΔE. E-irrep (E_g and E_u) phonons are doubly degenerate. Note that "0" denotes an entry that is precisely zero by symmetry, while "0.000" signifies a nonzero entry that has been rounded to zero. The energy shifts ΔE for A-irrep perturbed phonons are on the order of 10^{-4} μeV, and L_x for the O atom of the $A_{2g}^{(1)}$ phonon at 33.310 meV is $9 \times 10^{-9}\hbar$.

Irrep	E_0 (meV)	ΔE (μeV)	Cr L_z ($10^{-4}\hbar$)	O L_x ($10^{-4}\hbar$)	ρ (10^{-4})
E_g	36.458	−0.399	−2.087	−0.227	4.319
	43.739	−1.738	1.302	0.171	2.219
	49.602	−0.438	−0.073	0.175	1.104
	65.043	−0.124	−0.125	−0.037	2.592
	76.667	0.355	0.583	−1.471	10.547
E_u	38.209	−0.010	0.485	0.213	4.877
	55.803	−0.095	0.231	0.314	1.086
	67.431	1.161	1.537	−0.012	5.785
	76.041	0.023	−0.064	0.371	10.231
A_{1g}	36.326	0.000	0	0	0.225
	67.779	0.000	0	0	0.219
A_{1u}	51.723	0.000	0	0	0.335
	77.221	0.000	0	0	0.203
A_{2g}	33.310	0.000	0	0.000	0.727
	56.989	0.000	0	0.517	2.270
	83.594	0.000	0	−0.161	1.319
A_{2u}	50.565	0.000	0	0.090	1.784
	67.760	0.000	0	−0.604	2.212

The presence of magnetic moments in bulk Cr_2O_3 results in the breaking of i, σ_d, and S_6 symmetries associated with the bare phonons. Consequently, the original D_{3d} point group symmetry is reduced to D_3, leading to interirrep mixing between bare phonons of different irreps. Referring to the correlation table of the D_{3d} point group, we find that the E_g and E_u irreps combine to form the E irrep, the A_{1g} and A_{1u} combine to form the A_1 irrep, and the A_{2g} and A_{2u} irreps combine to form the A_2 irrep of D_3. An important question arises: How significant is this interirrep mixing, and to what extent does the spatial symmetry breaking due to the magnetic order impact the behavior of the phonons?

To address this question, we project the bare phonons belonging to irreps of the D_{3d} group onto the perturbed phonons. This allows us to determine the components of each irrep in D_{3d} that contribute to the given perturbed phonon. We introduce the concept of an irrep decomposition component denoted as $\rho_n(\mathrm{irrep})$, which is defined as

$$\rho_n(\mathrm{irrep}) = \left(\sum\nolimits_{m \in \mathrm{irrep}} |\langle u_m^{(0)}|M^{(\mathrm{pp})}|u_n\rangle|^2\right)^{\frac{1}{2}}, \quad (29)$$

where n is the label for the perturbed phonon mode, and m runs over bare phonons from a particular irrep. The last column of Table IV reports our results for $\rho_n(E_u)$ for $n \in E_g$ and vice versa, and similarly for the A_{1g}-A_{1u} and A_{2g}-A_{2u} components. In each case, the majority component [e.g., $\rho_n(E_g)$ for $n \in E_g$] is almost unity, so we list only the minority components. These are nonzero as expected, but we find them to be quite small, typically between 10^{-3} and 10^{-4}. This implies that the phonon sector exhibits only weak breaking of inversion symmetry, allowing us to continue to refer to the perturbed phonons as E_g-like or E_u-like.

2. Experimental implications: Raman and infrared activity

The experimental implication of the interirrep mixing is that the perturbed phonons will exhibit distinct Raman and IR activities compared to bare phonons, as summarized in Table V. Above the Néel temperature, where TRS is preserved, the symmetry of the phonons corresponds to that of the bare phonons, so that E_u phonons are IR active but Raman inactive. However, upon cooling the sample below the Néel temperature, E_u phonons undergo mixing with E_g phonons, resulting in the emergence of E_u-like perturbed phonons. These E_u-like phonons possess Raman activity (in addition to IR activity), as they technically belong to the E irrep of the D_3 point group. However, since the interirrep mixing is small, the Raman activity of the E_u-like phonons is relatively weak. Nonetheless, recent Raman measurements have confirmed the presence of these features [73]. In a similar way, the Raman-active E_g-like phonons acquire some small IR activity. Clearly, an approach such as ours, which treats the coupling of phonons and spins in a realistic and symmetry-consistent manner, is needed to describe these effects.

TABLE V. Raman and IR activities for bare and perturbed phonons. For perturbed phonons, the Irrep* column indicates the irrep of perturbed phonons labeled by irreps of D_{3d}, which is made possible by the weak interirrep mixing. In cases where a perturbed phonon exhibits both Raman and IR activity, the minor activity is presented within parentheses and is subordinate to the major activity.

Bare phonons		Perturbed phonons		
Irrep	Activity	Irrep	Irrep*	Activity
E_g	Raman	E	E_g-like	Raman (IR)
E_u	IR	E	E_u-like	IR (Raman)
A_{1g}	Raman	A_1	A_{1g}-like	Raman
A_{1u}		A_1	A_{1u}-like	Raman
A_{2g}		A_2	A_{2g}-like	IR
A_{2u}	IR	A_2	A_{2u}-like	IR

3. Atom-resolved phonon angular momentum

As mentioned earlier, inversion is no longer a symmetry in Cr_2O_3, but inversion times time reversal ($i\mathcal{T}$) remains a symmetry. This means that $i\mathcal{T}$ maps total angular momentum from $\vec{L}$ to $-\vec{L}$, resulting in $\vec{L} = \vec{0}$ for any nondegenerate single mode or for the sum over two degenerate modes. However, each atom can still possess a nonzero ARPAM defined by Eqs. (14) and (15) above. ARPAM is a pseudovector assigned to each atom and has the same symmetry as a local magnetic moment. The configuration of the local magnetic moment is determined by the magnetic space group, and this is also true for the ARPAM.

For Cr_2O_3, Cr and O atoms occupy Wyckoff positions $12c$ and $18e$, respectively. The possible configurations of ARPAM (and local magnetic moments) are listed in Table VI [based on the Bilbao crystallography server [74–76] (through the MWYCKPOS module [77])], indicating that Cr atoms can have only out-of-plane angular momentum L_z or $-L_z$, while O atoms can have only in-plane angular momentum in a way that respects C_3 symmetry. This is further supported by the numerical results presented in Table IV. In Fig. 5, we visualize the ARPAM for the $E_g^{(1)}$ perturbed phonon around 36 meV and the $A_{2g}^{(2)}$ perturbed phonon near 57 meV, where the L_z for Cr atoms and the in-plane angular momentum for O atoms are clearly visible.

It is important to note that there exists a gauge freedom for each E doublet, where the two degenerate modes can be unitarily mixed with each other through a U(2) matrix. Therefore, discussing ARPAM for each individual E mode is meaningless, as it is gauge dependent. However, the sum of ARPAM for the two degenerate E modes is gauge independent. To demonstrate this, let us consider an E doublet labeled by $n = \{1, 2\}$, where $L_{n,Iz}$ denotes the ARPAM for atom I along the z direction. Then, the sum of $L_{1,Iz}$ and $L_{2,Iz}$ is

$$\begin{aligned} &L_{1,Iz} + L_{2,Iz} \\ &= \hbar M_I \mathrm{Tr}\left[\begin{pmatrix} u_{1,Ix}^* & u_{1,Iy}^* \\ u_{2,Ix}^* & u_{2,Iy}^* \end{pmatrix}\begin{pmatrix} 0 & -i \\ i & 0 \end{pmatrix}\begin{pmatrix} u_{1,Ix} & u_{2,Ix} \\ u_{1,Iy} & u_{2,Iy} \end{pmatrix}\right] \\ &= 2\hbar M_I[\mathrm{Im}(u_{1,Ix}^* u_{1,Iy}) + \mathrm{Im}(u_{2,Ix}^* u_{2,Iy})], \end{aligned} \tag{30}$$

TABLE VI. Possible configurations of ARPAM for bulk Cr_2O_3 according to the magnetic space group $R\bar{3}'c'$. Cr atoms can have only out-of-plane angular momentum L_z or $-L_z$, while O atoms can have only in-plane angular momentum and must respect C_3 symmetry.

Atom	Wyckoff positions	ARPAM
Cr	$12c$	$(0,0,L_z)$, $(0,0,-L_z)$
O	$18e$	$\{I, C_3, C_3^2\}(L_x, 0, 0)$

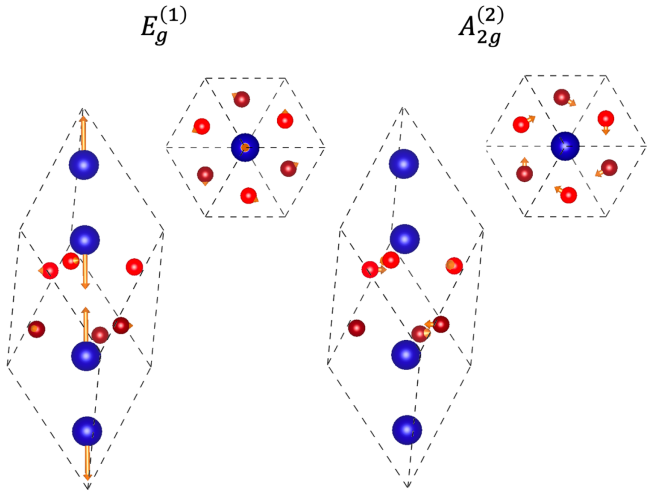

FIG. 5. ARPAM for two selected modes in bulk Cr_2O_3: $E_g^{(1)}$-like mode near 36 meV and $A_{2g}^{(2)}$-like mode near 57 meV. The ARPAM for the E_g-like mode is traced over two degenerate modes. The amplitude of ARPAM in this figure is amplified by a factor of 1000 compared to Fig. 6.

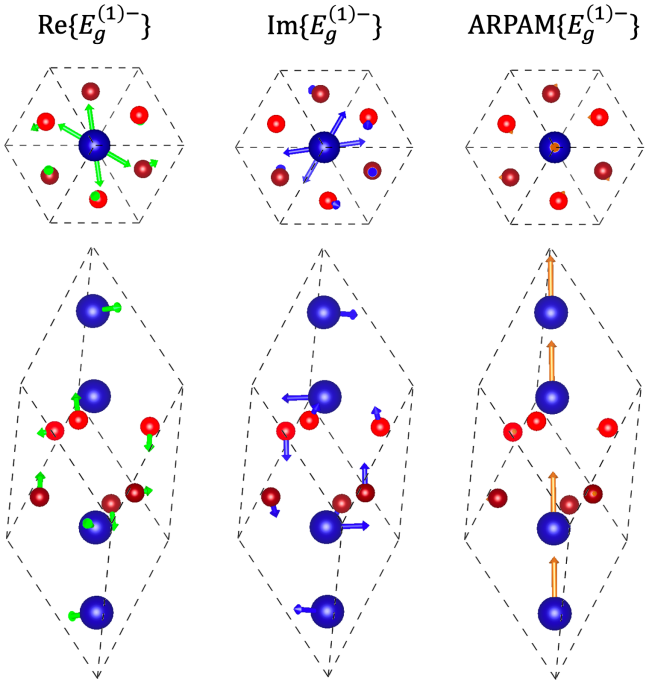

FIG. 6. The real and imaginary components, as well as ARPAM, of the chiral phonon $E_g^{(1)-}$ around 36 meV in Cr_2O_3. The Cr atoms are shown in blue, while the top-layer and bottom-layer O atoms are depicted in bright and dark red, respectively. The green vectors indicate the real part of the phonon displacement, the blue vectors indicate the imaginary part, and the brown vectors represent the ARPAM. The real parts of $E_g^{(1)+}$ are almost identical to $E_g^{(1)-}$, while its imaginary parts and ARPAM are almost opposite to those of $E_g^{(1)-}$.

which is the trace of a product of three matrices. While different gauges correspond to different bases for these matrices, they do not affect the trace, making $L_{1,Iz} + L_{2,Iz}$ a gauge-invariant quantity. This is also true for the x and y directions. The ARPAM for E-irrep perturbed phonons shown in Table IV is traced over the two degenerate modes in the doublet. For E modes with nonzero ARPAM, there is no gauge choice in the degenerate subspace where the phonon mode displacements can be expressed as purely real eigenvectors.

4. Chiral decomposition of E modes

Despite the fact that perturbed E phonons are always doubly degenerate, it is still worthwhile to decompose the doublet into two single E chiral phonons that respect C_3 symmetry individually and have complex eigenvalues. There are several reasons for this. First, these chiral phonons are excited by circular-polarized photons [45]. Second, they exhibit different energies in the presence of an external magnetic field along the z direction. Finally, these modes correspond to a special gauge choice in which each individual mode has the largest L_z magnitude. To decompose the E doublets, we diagonalize the C_3 matrix using the bases formed by two degenerate E modes. The resulting eigenvectors correspond to two E chiral phonons that respect C_3 symmetry individually. Since the two E modes together respect the C_3 symmetry, the C_3 matrix has to be a 2×2 unitary matrix, and is therefore diagonalizable.

We decompose the E_g-like perturbed phonons around 36 meV into two chiral phonons denoted as $E_g^{(1)+}$ and $E_g^{(1)-}$, and visualize their real parts, imaginary parts, and ARPAM in Fig. 6. The real parts of the two modes are almost identical to each other, while the imaginary parts are almost opposite. As a consequence, the ARPAMs of the two modes are also nearly opposite to each other. The PAMs for the $-$ and $+$ modes are $\pm 0.8593\hbar$, respectively. However, the ARPAMs of the two modes do not cancel out perfectly, and their sum is shown in the left panel of Fig. 5. Other E_g-like and E_u-like perturbed phonons can also be decomposed in the same manner.

5. Magnons

We now turn to a discussion of the magnons. As a reminder, bare magnons are solved as described in Sec. IV A 2, while perturbed magnons are magnonlike solutions of the EOM of the present approach. The energies of bare and perturbed magnons are presented in Table VII, and the numerical values for the matrices $K^{(\mathrm{ss})}$ and $G^{(\mathrm{ss})}$ describing the bare magnons are given in Appendix C.

We find that bare and perturbed magnons have almost identical energies, which results from the weak SOC for both the Cr and the O atoms. Since magnons belong to the E irrep, they must be doubly degenerate. These degenerate magnons can be decomposed into two magnons, each with $\chi(C_3)$ equal to ε or ε^*, following the same method we use

TABLE VII. Energies of the bare magnons (E_0) and corresponding shifts of perturbed magnons (ΔE) in bulk Cr_2O_3, as well as their E_g and E_u components defined in Eq. (29).

E_0 (meV)	ΔE (μeV)	$\rho(E_g)$	$\rho(E_u)$
2.423	−0.043	0.0386	0.9993
66.899	−0.045	0.6701	0.7423

with E phonons. Additionally, these magnons can also be excited by circular-polarized photons.

We next analyze the symmetries of magnons by considering the E_g and E_u components of each magnon mode, in a manner analogous to Eq. (29). Unlike the bare phonons, however, the bare magnons do not have well-defined parity, because the magnetic order strongly violates inversion symmetry. Therefore, we base our analysis on the eigenvectors of the anisotropy matrix $K^{(ss)}$ instead. Note that $K^{(ss)}$, being quadratic in the spin d.o.f., is real and symmetric, so that the symmetry operator $i\mathcal{T}$ behaves like i for $K^{(ss)}$. Thus, it has well-defined E_g and E_u eigenvectors that we denote as $|t_\mu\rangle$. Then, the E_g and E_u components of a general solution $|s_\mu\rangle$ are defined via

$$\rho_\mu(\text{irrep}) = \left(\sum\nolimits_{\nu\in\text{irrep}} |\langle t_\nu|s_\mu\rangle|^2\right)^{1/2}, \tag{31}$$

where both $|t_\nu\rangle$ and $|s_\mu\rangle$ are normalized. These ρ values can be used to quantify the extent to which the inversion symmetry is broken for magnons, and the numerical values are listed in Table VII. We find that the acoustic magnons, which have lower energies, are nearly E_u modes. However, the optical magnons have comparable $\rho(E_g)$ and $\rho(E_u)$ values, indicating that the inversion symmetry is strongly broken for these modes. This is not surprising, and is true also for the bare magnons, since the equations of motion for spin strongly violate TRS.

Note that we apply a 2% epitaxial strain to fix the sign of the magnetic anisotropic energy, which is related to the energy of acoustic magnons. Although the variation of the magnon energies is sensitive to strain, the impact of such variations on the phonon energy corrections is negligible. This is clarified by the perturbative analysis in Appendix D, particularly evident in Eq. (D20). Given that the energy difference between the E phonons and acoustic magnons is over 30 meV, a 1-meV variation in the magnon energy leads to a change of only about 3% in the phonon energy correction. Thus, changes in acoustic magnon energy, or the magnetic anisotropic energy, do not significantly influence the phonon energy corrections.

6. Summary of Cr_2O_3

In summary, our analysis shows that perturbed phonons possess D_3 symmetry, while bare phonons exhibit D_{3d} symmetry. The E-type irreps of both D_3 and D_{3d} are two dimensional, implying that there is no energy splitting despite the breaking of TRS. However, an E doublet can still be decomposed into two chiral phonons with different chiralities that respect C_3 symmetry. These chiral phonons can be excited by circular-polarized photons with different handedness, and their degeneracy will be lifted if an external magnetic field is present. Each perturbed phonon consists of components from two irreps of bare phonons, yet the level of interirrep mixing remains minimal. This characteristic implies that the inversion symmetry within the phonon sector is not strongly broken. Despite this minimal mixing, it is necessary to label perturbed phonons according to the irreps of the unitary subgroup of the magnetic point group. As a result, the infrared and Raman activity properties of these perturbed phonons differ from those of the bare phonons—a phenomenon that is confirmed by recent experimental observations. Magnons belong to the E irrep, and are therefore doubly degenerate. The magnons are mixtures of E_g and E_u sectors, indicating a strong inversion symmetry breaking for magnons.

C. Perturbed phonons and magnons in 2D systems

In Secs. IV A and IV B, we investigate chiral phonons in 3D systems, considering both FM and AFM cases. In this section, we shift our focus to 2D systems, specifically a monolayer of FM CrI_3 and a monolayer of AFM $VPSe_3$.

1. Chiral phonons in the monolayer CrI_3

Bulk CrI_3 has van der Waals gaps between layers, which allows it to be exfoliated to a 2D single layer while maintaining FM order [69]. In this section, we report our calculations of chiral phonons in monolayer CrI_3, with a focus on comparing the results with those in the bulk cases.

The crystal structure of monolayer CrI_3 is depicted in Fig. 7. The magnetic group $P\bar{3}1m'$ is a type-III black-white group, as is the case for bulk Cr_2O_3. The CrI_3 monolayer has higher structural symmetry than that of bulk CrI_3 due to the presence of dihedral mirrors (σ_d) and twofold rotations about an in-plane axis (C_2') that are absent in the bulk. This higher symmetry results in a structural D_{3d} point group, which is twice the size of the structural group S_6 of bulk CrI_3. However, the newly added symmetries are all anti-unitary in the presence of the FM spin ordering, so that the unitary group is again just S_6.

Thus, we again label the perturbed phonons at Γ using irreps of S_6, under which they decompose to $4A_g \oplus 4E_g \oplus 4A_u \oplus 4E_u$, where one A_u mode and two E_u modes are acoustic modes. Similar to bulk CrI_3, the E_g and E_u irreps in the S_6 point group correspond to two 1D complex irreps rather than a single 2D irrep. As a result, the E_g and E_u chiral phonons are no longer doubly degenerate and have energy splittings when compared to bare phonons. We refer to the E_g and E_u phonons as chiral phonons because they

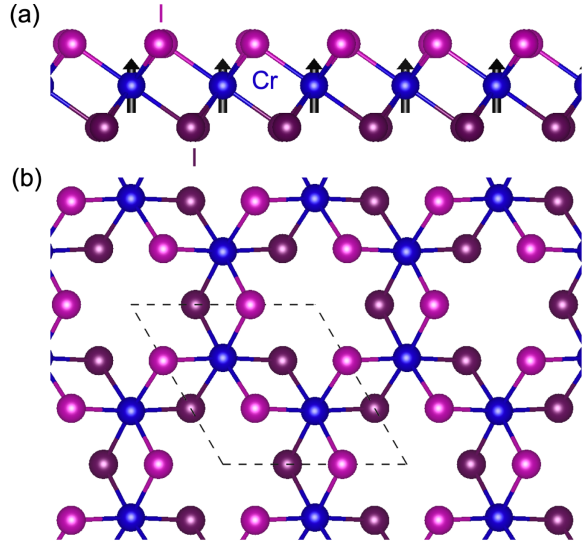

FIG. 7. Side (a) and top (b) views of the crystal structure of monolayer CrI_3, with a dashed line indicating the unit cell. Cr atoms are depicted in blue, while top-layer and bottom-layer I atoms are in bright and dark magenta, respectively. The black vectors indicate the magnetic moments, which are oriented along the z direction.

individually respect C_3 symmetry, but instead of having identity C_3 eigenvalues, they have complex eigenvalues (ε or ε^*). In Table VIII, we present the energies, angular momenta, and C_3 eigenvalues of the E_g and E_u chiral phonons, along with the energies of the bare phonons as a reference. Additionally, we include the results for magnons.

TABLE VIII. Energies, z-direction total PAM (L_z), and C_3 eigenvalue [$\chi(C_3)$] of E_g and E_u chiral phonons and magnons in monolayer CrI_3 calculated using the present approach. The bare phonon and magnon energies E_0 are included as a reference for the energy shift ΔE.

Irrep	E_0 (meV)	ΔE (meV)	$L_z(\hbar)$	$\chi(C_3)$
Phonons				
E_g	6.2343	−0.0028	0.1757	ε^*
		0.0033	−0.1762	ε
	12.6725	−0.0005	−0.2398	ε^*
		0.0007	0.2420	ε
	13.4436	−0.0010	0.2234	ε^*
		0.0011	−0.2250	ε
	30.1453	−0.0028	0.8408	ε^*
		0.0028	−0.8408	ε
E_u	10.0072	−0.0595	0.2535	ε
		−0.0014	−0.2314	ε^*
	14.2708	−0.0063	−0.7224	ε^*
		0.0450	0.7279	ε
	28.2112	0.0010	−0.9540	ε
		0.0036	0.9538	ε^*
Magnons				
E_g	0.9731	−0.0069		ε
E_u	10.5988	−0.0060		ε

Comparing Tables VIII and I, we observe that E_g chiral phonons in monolayer CrI_3 have a similar energy splitting to those in bulk CrI_3, but with larger PAM because the in-plane motion has been enhanced relative to out-of-plane motion. In monolayer CrI_3, the E_u chiral phonons around 10 meV have the largest energy splitting because they are closest in energy to the E_u magnon. Overall, the mechanisms for E_g and E_u chiral phonons in bulk and monolayer CrI_3 are similar despite differences in energy splittings and magnon energies.

In order to discuss the phonons belonging to the A irreps, it is essential to first determine the symmetries of the bare phonons. Similar to our argument in bulk Cr_2O_3, since $\sigma_d\mathcal{T}$ and $C_2'\mathcal{T}$ remain as symmetries, the bare phonons must possess D_{3d} symmetries instead of S_6. We find that the Γ-point bare phonons can be decomposed into $2A_{1g} \oplus 2A_{2g} \oplus 4E_g \oplus 1A_{1u} \oplus 3A_{2u} \oplus 4E_u$, wherein one A_{2u} mode and two E_u modes are acoustic. The presence of magnetic moments breaks the σ_d and C_2' symmetries of the bare phonons, which leads to interirrep mixing between the bare phonons of different irreps in the perturbed phonons. According to the correlation table of the D_{3d} point group, the A_{1g} and A_{2g} irreps combine to form the A_g irrep of S_6, while the A_{1u} and A_{2u} irreps combine to form A_u. However, as in bulk Cr_2O_3, the interirrep mixing in monolayer CrI_3 is found to be relatively weak, as demonstrated by the results presented in Table IX. This allows us to continue to refer to the perturbed phonons as, e.g., A_{1g}-like based on their predominant character. Nevertheless, it is important to emphasize that the correct labeling of zone-center phonons should consider the irreps of the S_6 group rather than the D_{3d} group.

Table IX contains the energies, angular momenta, and interirrep mixing of A_g and A_u perturbed phonons. Bare phonon energies are also included as a reference for the energy shifts. By comparing Tables II and IX, we observe that the perturbed phonons from the A irreps in both bulk and monolayer CrI_3 exhibit small energy shifts and have a small PAM, indicating a weak effect of the $G^{(\mathrm{pp})}$ matrices in both cases.

TABLE IX. Energies, total z-direction PAM (L_z), and interirrep mixing for A-irrep perturbed phonons in monolayer CrI_3. "Irrep" labels are those of the parent bare phonons, whose energies E_0 are included as a reference for the energy shift ΔE.

Irrep	E_0 (meV)	$\Delta E(10^{-8}$ meV)	$L_z(10^{-4}\hbar)$	ρ_n (10^{-4})
A_{1g}	9.47	−6.3	−2.07	1.47
	16.12	−67.4	1.50	2.30
A_{2g}	10.92	2.2	2.22	1.72
	26.98	125.4	−2.10	3.77
A_{1u}	16.67	−5.0	−2.49	1.37
A_{2u}	7.02	−3.7	0.94	0.48
	32.69	27.0	0.49	1.49

Concerning the magnons, we find that the energy of the optical magnon in monolayer CrI_3 is lower than in the bulk. This is attributable to the absence of ferromagnetic interlayer exchange in the monolayer [78]. In contrast, the energy for the acoustic magnon is greater than that in the bulk. As the acoustic magnon energy is related to the magnetic anisotropy energy (MAE), this suggests a greater MAE for monolayer CrI_3. This observation agrees with findings from another study [79], where the generalized-gradient approximation to the exchange-correlation functional was used [80]. The numerical values for the matrices $K^{(ss)}$ and $G^{(ss)}$ are provided in Appendix C.

In summary, as is the case for the chiral phonons in bulk CrI_3, the E_g and E_u chiral phonons in monolayer CrI_3 are no longer doubly degenerate and possess significant angular momentum. The A_g and A_u perturbed phonons exhibit small energy shifts with respect to the bare phonons and acquire nonzero angular momentum. However, unlike the bulk case, A_g and A_u perturbed phonons in monolayer CrI_3 exhibit interirrep mixing due to the symmetry reduction caused by the presence of magnetic order. From the perspective of optical activity, the A_{2g}-like perturbed phonons are weakly Raman active, since they contain some components from the A_{1g} sector, whereas the A_{1u}-like perturbed phonons acquire some IR activity due to components from A_{2u}.

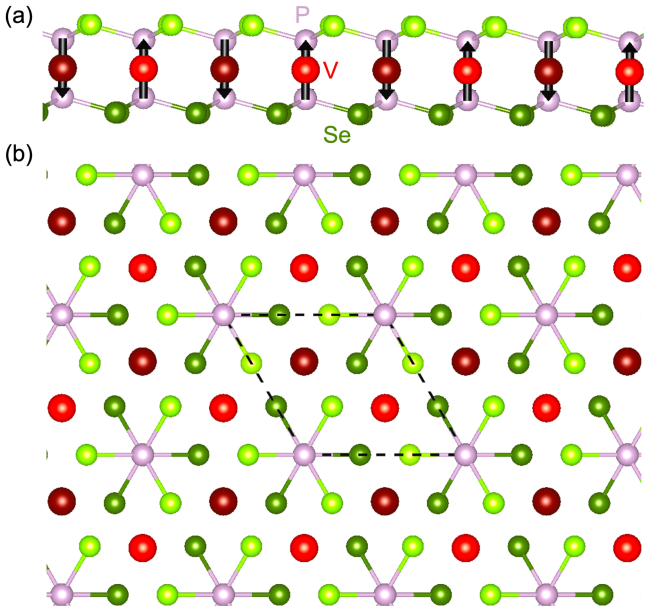

FIG. 8. Side (a) and top (b) views of the crystal structure of monolayer $VPSe_3$, with a dashed line indicating the unit cell. Bright and dark shades denote V atoms with spin-up and -down, respectively. Purple atoms represent P atoms, while top-layer and bottom-layer Se atoms are in bright and dark green, respectively. The magnetic moments, oriented along the z direction, are denoted by black vectors.

2. *Phonons in monolayer* $VPSe_3$

In this section, we investigate the phonons of a VPSe3 monolayer, which is a 2D AFM insulator. It is predicted to have a Néel-type AFM structure [64], with the magnetic moment oriented along the z direction. The crystal structure of monolayer $VPSe_3$ is depicted in Fig. 8. The magnetic space group is $P\bar{3}'1m$, which is again a type-III black-white group. The structural point group is D_{3d}, but the magnetic moments from V atoms break both inversion (i) and twofold-rotational (C_2') symmetries, reducing the unitary point group to C_{3v}. The threefold rotation (C_3) and dihedral mirror (σ_d) remain symmetries of the magnetic group, together with operations $i\mathcal{T}$, $C_2'\mathcal{T}$, and $S_6\mathcal{T}$.

According to the character table for the C_{3v} point group, the E irrep is a true 2D irrep, i.e., not a complex-conjugate pair of 1D irreps. Therefore, perturbed phonons belonging to E irreps must be doubly degenerate, which is confirmed by the numerical results in Table X. The energies of the perturbed phonons are described by energy shifts ΔE with respect to the bare phonon energies (E_0).

The $VPSe_3$ monolayer maintains $i\mathcal{T}$ symmetry similar to Cr_2O_3. This symmetry forbids the existence of a nonzero total PAM but permits the presence of nonzero ARPAMs. The magnetic space group of $VPSe_3$ is $P\bar{3}'1m$, with V, P, and Se atoms occupying the $2c$, $2e$, and $6k$ Wyckoff positions, respectively. We find that V atoms possess only nonzero L_z, Se atoms can have only nonzero in-plane $\mathbf{L}$, and P atoms cannot carry angular momentum. The ARPAMs for the perturbed phonons traced over the subspace of degenerate doublet for phonons with E irreps are provided in Table X. It is possible to further decompose the doublets from E irreps into two chiral phonons, which individually respect the C_3 symmetry but have different complex eigenvalues.

Building on our earlier discussion, similar to monolayer CrI_3 and Cr_2O_3, the D_{3d} symmetry is preserved by $K^{(pp)}$ and $M^{(pp)}$ in monolayer $VPSe_3$, allowing us to use irreps of D_{3d} to label zone-center bare phonons. These bare phonons decompose to $5E_g \oplus 5E_u \oplus 3A_{1g} \oplus 4A_{2u} \oplus 1A_{1u} \oplus 2A_{2g}$, with one A_{2u} and two E_u modes being acoustic modes. However, due to the presence of magnetic moments on V atoms, i and C_2' symmetries are broken, reducing the symmetry to C_{3v} and requiring the use of irreps from this point group to label perturbed phonons instead of D_{3d}. The interirrep mixing resulting from the symmetry reduction can be determined from the correlation table, which shows that E_g and E_u bare phonons form E perturbed phonons, A_{1g} and A_{2u} bare phonons form A_1 perturbed phonons, and A_{2g} and A_{1u} bare phonons form A_2 perturbed phonons. As in the cases of monolayer CrI_3 and Cr_2O_3, the interirrep mixing caused by the magnetic order is small. Thus, we still refer to the perturbed phonons as E_g-like, etc., but again the correct labeling of those perturbed phonons should involve the irrep of C_{3v} rather than those of D_{3d}.

TABLE X. Bare phonon irreps, energies, ARPAM of V atoms in the z direction (V L_z), ARPAM of Se atoms in the y direction (Se L_y), and interirrep mixing (ρ) of perturbed phonons in monolayer $VPSe_3$. Bare phonon energies E_0 are included as a reference for energy shifts ΔE. The E-irrep phonons are doubly degenerate. The energy shifts ΔE for A-irrep perturbed phonons are on the order of $10^{-5}\mu$eV.

Irrep	E_0 (meV)	ΔE (μeV)	V L_z ($10^{-4}\hbar$)	Se L_y ($10^{-4}\hbar$)	ρ (10^{-4})
E_g	12.790	0.052	−0.238	0.008	0.384
	15.102	0.230	0.337	0.707	4.161
	20.127	0.049	−0.055	−0.441	1.116
	27.728	−0.001	−9.280	−0.145	6.013
	53.837	0.016	−0.055	−0.323	26.994
E_u	14.526	0.033	−0.453	−0.620	4.269
	18.125	0.049	0.077	0.189	1.029
	30.765	−0.005	11.104	0.171	6.768
	53.697	−0.019	0.039	0.245	26.945
A_{1g}	18.743	0.000	0	−0.224	1.154
	25.490	0.000	0	0.050	1.032
	62.327	0.000	0	−0.012	0.357
A_{2u}	16.287	0.000	0	0.280	1.101
	32.081	0.000	0	−0.104	0.624
	37.856	0.000	0	−0.142	0.859
A_{1u}	16.625	0.000	0	0	0.581
A_{2g}	8.955	−0.000	0	0	0.307
	30.688	0.000	0	0	0.220

The interirrep mixing ρ is defined in the same manner as with Cr_2O_3 using Eq. (29), and the results are presented in Table X. The interirrep mixing leads to anomalous Raman and IR activities as well. For example, the A_{1g}-like and E_g-like perturbed phonons, which are strongly Raman active, now acquire small IR activities, while IR-active A_{2u}-like and E_u-like perturbed phonons acquire small Raman activities. The A_{2g}-like and A_{1u}-like perturbed phonons remain silent in both Raman and IR activities.

In addition, we study the energies of bare and perturbed magnons. Both bare and perturbed magnons are doubly degenerate as they belong to the E irrep. The bare magnon energy is found to be 8.58 meV, while the energy shift of the perturbed magnon is −0.81 μeV, which is more significant than in Cr_2O_3. This can be attributed to the larger SOC in $VPSe_3$. We further analyze the symmetry of the perturbed magnon by decomposing it into E_g and E_u eigenmodes of $K^{(\mathrm{ss})}$. Our findings reveal that $\rho(E_u) = 0.9992$, while $\rho(E_g) = 0.0405$, indicating that the magnon is almost entirely of E_u symmetry, similar to the acoustic magnon in Cr_2O_3. The numerical values for the matrices $K^{(\mathrm{ss})}$ and $G^{(\mathrm{ss})}$ are provided in Appendix C.

To summarize, we computed the perturbed phonons of monolayer VPSe3. While bare phonons retain D_{3d} symmetry, perturbed phonons possess only C_{3v} symmetry due to the presence of magnetic moments. As in the case of Cr_2O_3, the E-irrep in C_{3v} is a 2D irrep, preserving degeneracy despite the broken TRS. The total PAM of each perturbed phonon is zero due to $i\mathcal{T}$ symmetry, but perturbed phonons can possess nonzero ARPAM. Moreover, we also investigate the energies of bare and perturbed magnons, finding that the energy shift of magnons is greater than in Cr_2O_3. Although the magnon is almost entirely of E_u symmetry, the E_g-E_u mixing in the magnon sector is more pronounced than in the phonons.

V. DISCUSSION

A. Role of spin-orbit coupling

SOC is essential to the physics described above. We identify three matrices, namely, $K^{(\mathrm{sp})}$, $G^{(\mathrm{sp})}$, and $G^{(\mathrm{pp})}$, all of which either violate TRS or mediate the interaction between phonons and magnons. Here we show that in collinear systems such as those considered here, all three of these matrices vanish in the absence of SOC. Since these matrices control the splittings of degenerate phonon modes, it follows that these splittings also vanish without SOC. This is demonstrated here using formal arguments and then confirmed via numerical calculations on bulk CrI_3.

In the absence of SOC, the presence of global spin rotational symmetry implies that the exchange interactions are of pure Heisenberg form $H = \sum_{\langle ij\rangle} J_{ij}\mathbf{S}_i \cdot \mathbf{S}_j$, where the J_{ij} depend on the atomic coordinates. Spin-phonon coupling in noncollinear systems is often described in terms of exchange striction, i.e., the first-order changes of J_{ij} with atomic displacements (see, e.g., Ref. [81]). However, such variations of J_{ij} do not induce any spin canting in an SOC-free collinear system. This follows because the energy is stationary with respect to canting of any spin, since $\delta H = \sum_{\langle ij\rangle} J_{ij}[\mathbf{S}_i \cdot \delta\mathbf{S}_j + \delta\mathbf{S}_i \cdot \mathbf{S}_j]$, and $\mathbf{S}_i$ and $\delta\mathbf{S}_j$ are orthogonal in a collinear spin system.

A complementary point of view comes from noting that the spinor wave functions are separable into real spatial wave functions with pure spin-up or spin-down character in an SOC-free collinear magnet. This remains true as atoms are displaced, so that there is no induced spin canting. This observation also explains why $G^{(\mathrm{pp})}$ vanishes. For example, consider three structural configurations, a reference 0 and configurations with displacements δq_i and δq_j. The Berry phase

$$\Phi_{ij} = -\mathrm{Im}\ \ln[\langle\psi_0|\psi_{\delta q_i}\rangle\langle\psi_{\delta q_i}|\psi_{\delta q_j}\rangle\langle\psi_{\delta q_j}|\psi_0\rangle] \quad (32)$$

clearly vanishes, since all inner products are real.

The argument for the vanishing of $G^{(\mathrm{sp})}$ is slightly more subtle. This time, one of the displacements, say, δq_j, is replaced by a spin canting δs_j of one spin. The spin system is no longer collinear, but it is still coplanar. In this case, the spinors can be represented using Pauli matrices σ_3 and σ_1 to span the plane in which the spins lie. Both of these Pauli matrices are real, so the overall spatial-spinor wave

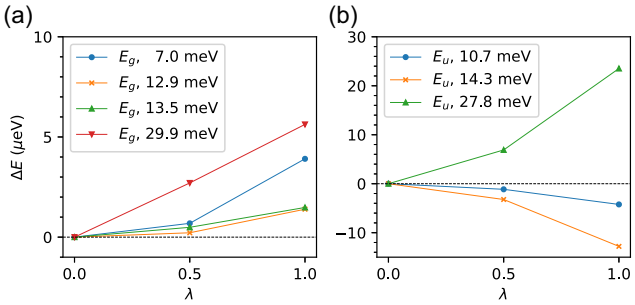

FIG. 9. Energy splittings (ΔE) for the E_g chiral phonon modes (a) and E_u chiral phonon modes (b) in bulk CrI_3, plotted as a function of the spin-orbit coupling strength scaling factor (λ). The ΔE represents the energy difference between the "+" mode and the "−" mode near that energy.

functions remain real, and the Berry phase around the loop remains zero.

To confirm these conclusions, we repeat the calculation of the spin splittings in bulk CrI_3 while varying the strength of the SOC used in the first-principles calculations. This adjustment requires the introduction of a multiplicative factor in the computational code, followed by recompilation. Figure 9 shows the variation of the phonon energy splittings ΔE with the scaling factor λ for the SOC, where $\lambda = 1$ is the physical strength. Clearly, the splittings get smaller as λ is reduced and vanish at $\lambda = 0$, consistent with our expectations.

We find that $K^{(\mathrm{sp})}$, $G^{(\mathrm{sp})}$, and $G^{(\mathrm{pp})}$ have linear as well as quadratic terms in λ (with the exception of the $K^{(\mathrm{sp})}$ coupling to acoustic magnons). The quadratic terms are dominant in most cases in Fig. 9, although the linear behavior dominates for the highest-energy E_g mode.

We emphasize that these conclusions hold for collinear spin systems. While we do not study noncollinear systems in this work, we fully expect the present approach to apply in that case. In particular, exchange striction will induce bilinear couplings between atomic displacements and spin cantings as captured by our spin-phonon Hession $K^{(\mathrm{sp})}$, even in the absence of SOC. The role of SOC in the spin-phonon coupling of noncollinear systems may be an interesting avenue for future research.

B. Connection with experiment

Before concluding this paper, we would like to provide some comments on experiments. In materials where chiral phonons exhibit an energy splitting, it is possible to measure this splitting using Raman or IR spectroscopy. Since the splittings for E_g chiral phonons are usually small, it may be more feasible to measure splittings of E_u chiral phonons using IR spectroscopy. Additionally, circular-polarized photons with different handedness can excite chiral phonons with different chiralities, and observing the peak shift on the spectrum measured using different circular-polarized photons is possible. Another approach is to measure the magnetic moment of the excited chiral phonon using circular-polarized photons, which can be applicable regardless of the presence of energy splitting. Light-induced demagnetization has been observed in many materials, including bulk CrI_3 [82], due to electronic excitation of crystal field levels. However, by adjusting the energy of photons to resonate with a chiral phonon but not to excite electrons, one can selectively probe the chiral phonons because the energy differences between crystal field levels or semicore levels are typically larger than phonon energies. Therefore, electronic excitations can be avoided when probing chiral phonons selectively.

VI. CONCLUSION

Based on a Lagrangian formulation, we developed a theoretical formalism and computational methodology to determine adiabatic dynamics in systems with multiple slow degrees of freedom. Our computational methodology is based on static constrained DFT calculations of Hessians and Berry curvatures with respect to the slow parameters in order to extract the semiclassical dynamics. This framework constitutes a general and computationally efficient approach that does not require explicit time-dependent *ab initio* calculations as in, e.g., TDDFT, or other specialized capabilities beyond those commonly found in, or easily added to, widely available DFT codes. We demonstrated the utility of this methodology by applying it to phonons and spins (magnons) in magnetic insulators, as the dynamics of each is generally on the same energy scale. This represents a more systematic way of treating spin-phonon dynamics compared to conventional approaches which rely on building spin models and parametrizing their dependence on atomic displacements.

Specifically, we showed that the inclusion of the Hessians and Berry curvatures involving spin and phonon d.o.f. are required to accurately describe the often-neglected effects of TRS breaking on phonon modes at the zone center. Results for four case-study materials were presented, covering both FM and AFM ordering, as well as 2D and 3D materials. FM CrI_3 (both 3D bulk and 2D monolayer) exhibits energy splittings of its E-type modes (which are doubly degenerate under TRS) at the zone center. This results in chiral phonons exhibiting circular atomic motion leading to a significant phonon angular momentum. In AFM Cr_2O_3 (3D bulk) and $VPSe_3$ (2D monolayer), the E-type modes remain doubly degenerate, but the inversion symmetry breaking from the magnetic order results in modes with mixed E_g and E_u character. The angular momentum of a phonon in these materials is zero in total, but can exhibit well-defined nonzero atom-resolved contributions. In addition, the mixing of E_g and E_u modes implies that the Raman modes acquire some small IR character and vice versa, a feature that is open to experimental confirmation.

This work opens up various directions for future study. The general methodology will be useful in any material

with interesting dynamics involving multiple slow d.o.f. Specifically in the area of spin-phonon dynamics, it allows the search for materials with large splittings of chiral modes, due, for example, to large SOC or approximate degeneracies between phonon and magnon branches. It also motivates the exploration of dynamics of materials with more complicated magnetic structures, such as non-collinear or so-called altermagnetic [83,84] orders. Finally, we focused here on zone-center modes, but the methodology shows promise for being generalized for computing the coupled spin-phonon dynamics across the Brillouin zone, which is relevant for the thermal Hall effect.

Overall, we expect that the developments in this work will allow efficient and accurate calculations of generalized adiabatic dynamics, and thus the exploration of much resulting novel physical phenomena in spin-phonon coupled systems and beyond.

ACKNOWLEDGMENTS

This work was supported by NSF Grants No. DMR-1954856 (D. V.) and No. DMR-2237674 (C. E. D.). M. S. acknowledges support from Ministerio de Ciencia e Innovación (MCIN/AEI/10.13039/501100011033) through Grant No. PID2019–108573 GB-C22, from Severo Ochoa FUNFUTURE center of excellence (CEX2019-000917-S), from Generalitat de Catalunya (Grant No. 2021 SGR 01519), and from the European Research Council under the European Union's Horizon 2020 research and innovation program (Grant Agreement No. 724529). The authors thank Sinisa Coh for helpful discussions in the early stage of this work. S. R. and D. V. acknowledge the valuable discussions with Girsh Blumberg and Shangfei Wu, as well as their kind permission to reference their unpublished Raman measurement data. S. R. acknowledges the support of Predoctoral Researcher Program of Center for Computational Quantum Physics at the Flatiron Institute. The Flatiron Institute is a division of the Simons Foundation.

APPENDIX A: DERIVATION OF PHONON HAMILTONIAN

In this section, we review the adiabatic theory of phonons with TRS breaking, which is based on a Hamiltonian formalism first introduced by Mead and Truhlar (MT) [25]. In the MT approach, the only slow variables are nuclear coordinates. One can start from the full Hamiltonian for a system with electrons and nuclei, which is [85]

$$\begin{aligned} H_{\mathrm{tot}} &= T_{\mathrm{N}}(R) + T_{\mathrm{e}}(r) + V(r,R), \\ T_{\mathrm{N}}(R) &= -\sum_I \frac{\hbar^2 \nabla_I^2}{2M_I}, \\ T_{\mathrm{e}}(r) &= -\sum_i \frac{\hbar^2 \nabla_i^2}{2m}, \end{aligned} \tag{A1}$$

where $T_{\mathrm{N}}(R)$ and $T_{\mathrm{e}}(r)$ are nuclear kinetic energy and electronic kinetic energy, respectively. $V(r,R)$ represents the total electrostatic interactions between electrons, nuclei, and electron-nuclei interactions, which includes the effects of spin-orbit coupling. R is the nuclear coordinate, and r is electronic. I runs over nuclei, and i runs over electrons. $Z_I e$ is the positive charge for the nucleus I. The Schrödinger equation for the wave function $\Psi(r,R)$ is

$$[T_{\mathrm{N}}(R) + T_{\mathrm{e}}(r) + V(r,R)]\Psi(r,R) = W\Psi(r,R), \tag{A2}$$

where W is the energy for the whole system.

Now, one can implement the Born-Oppenheimer approximation [24], which treats R as a slow variable and assumes the electronic dynamics is always much faster than nuclear vibrations. As a consequence, the wave function can be separated into an electronic and nuclear part

$$\Psi(r,R) = \psi(r;R)\chi(R), \tag{A3}$$

where the electronic part $\psi(r;R)$, which satisfies

$$[T_{\mathrm{e}}(r) + V(r,R)]\psi(r;R) = \epsilon(R)\psi(r;R), \tag{A4}$$

is the normalized ground-state wave function with respect to the nuclear coordinates R. $\psi(r;R)$, $V(r,R)$, and $\epsilon(R)$ depend on R parametrically. One should also notice that $\psi(r;R)$ has a U(1) gauge freedom; namely,

$$\tilde{\psi}(r;R) = e^{i\phi(R)}\psi(r;R) \tag{A5}$$

is also a solution to Eq. (A4), where $e^{i\phi(R)}$ is an R-dependent phase factor. Plugging Eq. (A3) into Eq. (A2), multiplying $\psi^*(r;R)$ from the left, and integrating over r gives

$$\begin{aligned} &\left[\sum_{I\alpha} \frac{(P_{I\alpha} - \hbar A_{I\alpha})^2}{2M_I} + \epsilon(R) + \Lambda(R)\right]\chi(R) = W\chi(R), \\ &\Lambda(R) = \frac{\hbar^2}{2M_I}(\langle \partial_{I\alpha}\psi(R)|\partial_{I\alpha}\psi(R)\rangle - A_{I\alpha}^2), \\ &A_{I\alpha} = i\langle \psi(R)|\partial_{I\alpha}\psi(R)\rangle, \end{aligned} \tag{A6}$$

where $A_{I\alpha}$ is a Berry potential with respect to nuclear displacements thus called "nuclear Berry potential." As first pointed out by Mead and Truhlar [25], it is not always possible to make $A_{I\alpha}$ zero by tuning the R-dependent phase $\phi(R)$ in Eq. (A5). Here the Dirac bra-ket notation is only for the electronic degree of freedom r. Note that $\Lambda(R)$ can be rewritten as

$$\begin{aligned} \Lambda(R) &= \frac{\hbar^2}{2M_I}\langle \partial_{I\alpha}\psi(R)|Q|\partial_{I\alpha}\psi(R)\rangle, \\ Q &= 1 - |\psi(R)\rangle\langle\psi(R)|; \end{aligned} \tag{A7}$$

therefore, $\Lambda(R)$ is gauge independent. $\Lambda(R)$ is related to the expectation value of electronic kinetic energy $\langle T_e(r)\rangle$ to the order of m/M, where m and M are the electronic and nuclear mass, respectively. As $\langle T_e(r)\rangle$ is included in $\epsilon(R)$, we have $\Lambda(R) \ll \epsilon(R)$. Since we focus on broken TRS in this work, it is worth noting that $\Lambda(R)$ does not break TRS. Therefore, we disregard $\Lambda(R)$ in this work. In addition, we consider only nuclear d.o.f. in this section. To simplify the notation, we introduce a composite index l for $I\alpha$, which is used to label nuclear d.o.f.

Now we are ready to write down the effective Hamiltonian for phonons, which is

$$H_{\text{eff}} = \sum_l \frac{(P_l - \hbar A_l)^2}{2M_l} + \epsilon(R), \tag{A8}$$

and the EOM is

$$\dot{R}_l = \frac{\partial H}{\partial P_l} = \frac{P_l - \hbar A_l}{M_l}, \tag{A9}$$

$$\begin{aligned}\dot{P}_l &= -\frac{\partial H}{\partial R_l} = \sum_m \frac{P_m - \hbar A_m}{M_m}(\partial_l A_m) - \partial_l \epsilon(R), \\ &= \hbar \sum_m \dot{R}_m \partial_l A_m - \partial_l \epsilon(R),\end{aligned} \tag{A10}$$

where ∂_l denotes $\partial/\partial R_l$. Combining Eqs. (A10) and (A9), one can get

$$\begin{aligned}M_l \ddot{R}_l &= \dot{P}_l - \hbar \dot{A}_l \\ &= -\partial_l \epsilon(R) + \hbar \sum_m \dot{R}_m (\partial_l A_m - \partial_m A_l),\end{aligned} \tag{A11}$$

where we use the relation $\dot{A}_l(R) = (\partial_m A_l)\dot{R}_m$ in the second line. By introducing

$$G_{lm} = \hbar \Omega_{lm} = \hbar(\partial_l A_m - \partial_m A_l), \tag{A12}$$

where the Ω_{lm} is the nuclear Berry curvature, which is gauge invariant, Eq. (A11) can be written in a compact form as

$$M_l \ddot{R}_l = -\partial_l \epsilon(R) + \sum_m G_{lm}(R)\dot{R}_m. \tag{A13}$$

Equation (A13) is equivalent to Eq. (9) for the case that Q_i corresponds to a nuclear d.o.f. However, they are obtained using Hamiltonian and Lagrangian formalism, respectively. In this way, starting with a full quantum theory, a semiclassical theory of the dynamics has been derived.

APPENDIX B: FROM PRESENT APPROACH TO SPIN-PHONON MODEL

It is mentioned in Sec. II C that the spin-phonon model in Ref. [33] includes only $G^{(\text{ss})}$ and neglects all other Berry curvature tensors, which we illustrate below. If we let $G^{(\text{pp})}$, $G^{(\text{ps})}$, and $G^{(\text{sp})}$ be all zero, then we get the EOM for the spin-phonon model as

$$\begin{aligned}M^{(\text{pp})}|\ddot{u}\rangle &= -K^{(\text{pp})}|u\rangle - K^{(\text{ps})}|s\rangle, \\ G^{(\text{ss})}|\dot{s}\rangle &= K^{(\text{sp})}|u\rangle + K^{(\text{ss})}|s\rangle.\end{aligned} \tag{B1}$$

These equations can be solved exactly. However, to establish a connection with the minimal spin-phonon model proposed in Ref. [33], we can derive Eq. (6) in that reference from Eq. (B1).

We introduce the new phonon vector $|v\rangle = M^{1/2}|u\rangle$, so that $M^{(\text{pp})}$ no longer appears in the EOM explicitly. Consequently, Eq. (B1) can be rewritten as

$$|\ddot{v}\rangle = -\tilde{K}^{(\text{pp})}|v\rangle - \tilde{K}^{(\text{ps})}|s\rangle, \tag{B2}$$

$$G^{(\text{ss})}|\dot{s}\rangle = \tilde{K}^{(\text{sp})}|v\rangle + K^{(\text{ss})}|s\rangle, \tag{B3}$$

where $\tilde{K}^{(\text{pp})} = [M^{(\text{pp})}]^{-1/2}K^{(\text{pp})}[M^{(\text{pp})}]^{-1/2}$, $\tilde{K}^{(\text{ps})} = [M^{(\text{pp})}]^{-1/2}K^{(\text{ps})}$, and $\tilde{K}^{(\text{sp})} = K^{(\text{sp})}[M^{(\text{pp})}]^{-1/2}$. Note that $\tilde{K}^{(\text{pp})}$ is the dynamical matrix.

Now we focus only on bulk CrI_3 and include one bare phonon doublet and the magnon from the same irrep in the formalism. We introduce the unperturbed solution of Eqs. (B2) and (B3), which we refer to as bare phonons and magnons, as

$$\tilde{K}^{(\text{pp})}|v_\pm\rangle = \omega_{\text{p}}^2|v_\pm\rangle, \tag{B4}$$

$$K^{(\text{ss})}|s_\pm\rangle = -i\omega_{\text{m}}G^{(\text{ss})}|s_\pm\rangle, \tag{B5}$$

where ω_{p} and ω_{m} are energies for bare phonons and magnons, respectively. The $\pm$ subscript in $|v_\pm\rangle$ and $|s_\pm\rangle$ represents the left- and right-hand circular-polarized modes. Specifically, for the E_g magnon, we have $|s_\pm\rangle = \frac{1}{2}(1, \mp i, 1, \mp i)^T$, where the first two components correspond to the x and y components of the reduced spin unit vector of the first Cr atom, and the last two components correspond to the second Cr atom. Similarly, for the E_u magnon, we have $|s_\pm\rangle = \frac{1}{2}(1, \mp i, -1, \pm i)^T$.

If we adopt the assumption made in Ref. [33], which states that

$$G = -S\begin{pmatrix} 0 & 1 & 0 & 0 \\ -1 & 0 & 0 & 0 \\ 0 & 0 & 0 & 1 \\ 0 & 0 & -1 & 0 \end{pmatrix}, \tag{B6}$$

we can verify that

$$\langle s_\pm|G^{(\mathrm{ss})}|s_\pm\rangle = \pm iS, \tag{B7}$$

regardless of whether $|s_\pm\rangle$ belongs to the E_g or E_u magnons. However, in our numerical calculations for CrI_3, we observe that the effective spin S for E_g and E_u magnons is slightly different. The numerical values for these effective spins are provided in Appendix C.

According to symmetry considerations, modes with different chiralities should not mix under any of the matrices in Eq. (B1). Therefore, we have

$$\langle s_\pm|K^{(\mathrm{sp})}|v_\pm\rangle = \gamma, \tag{B8}$$

$$\langle s_\pm|K^{(\mathrm{sp})}|v_\mp\rangle = 0, \tag{B9}$$

where γ represents the spin-phonon coupling strength. It is always possible to add a phase to either $|s_\pm\rangle$ or $|v_\pm\rangle$ in order to make γ real. Therefore, we assume γ to be real, resulting in $\langle s_\pm|K^{(\mathrm{sp})}|v_\pm\rangle = \langle v_\pm|K^{(\mathrm{ps})}|s_\pm\rangle = \gamma$.

We can expand $|v\rangle$ and $|s\rangle$ in the bases of $|v_\pm\rangle$ and $|s_\pm\rangle$ as

$$|v\rangle = x_\pm|v_\pm\rangle, \tag{B10}$$

$$|s\rangle = s_\pm|s_\pm\rangle, \tag{B11}$$

where $x_\pm$ and $s_\pm$ are coefficients representing the magnitudes of the contributions from the corresponding basis vectors. In the minimal spin-phonon model, it is assumed that the mixing between different E_g doublets is negligible. However, in reality, this mixing, which is mediated by magnons, plays a crucial role in explaining why the angular momenta of the two circular-polarized modes do not cancel out exactly. A more detailed analysis of this mixing based on the perturbation approach can be found in Appendix D 1.

By multiplying $\langle v_\pm|$ to Eq. (B2) and substituting Eqs. (B4), (B10), and (B8), we obtain

$$(\omega_\mathrm{p}^2 - \omega^2)x_\pm = -\gamma s_\pm. \tag{B12}$$

Similarly, by multiplying $\langle s_\pm|$ by Eq. (B3) and substituting Eqs. (B5), (B7), and (B8), we get

$$(\pm\omega_s - \omega)s_\pm = \mp S^{-1}\gamma x_\pm. \tag{B13}$$

Thus, we have successfully derived Eq. (6) in Ref. [33].

Although Eq. (B1) is derived from an adiabatic Lagrangian formalism, we aim to demonstrate that it can also emerge from the undamped Landau-Lifshitz equation [52]. In its original form, the Landau-Lifshitz equation is presented as

$$\frac{d\vec{M}}{dt} = -\gamma\vec{M}\times\frac{dH}{d\vec{M}}, \tag{B14}$$

where H is the Hamiltonian, $dH/d\vec{M}$ is the effective magnetic field, and γ represents the gyromagnetic ratio, which is the ratio of the magnetic moment $\vec{M}$ to its corresponding angular momentum $\vec{S}$. As the dynamic variable in our study is the unit vector of spin $\vec{s} = \vec{S}/S$, we can recast Eq. (B14) in terms of $\vec{s}$ as

$$S\frac{d\vec{s}}{dt} = -\vec{s}\times\frac{dH}{d\vec{s}}. \tag{B15}$$

Equation (B15) can be rewritten in component form as

$$S\frac{ds_\alpha}{dt} = -\epsilon_{\alpha\beta\gamma}s_\beta\frac{dH}{ds_\gamma}, \tag{B16}$$

where α, β, and γ span over the Cartesian coordinates. Given that the spin deviation from the z direction is small, we can make a simplification on the right-hand side of this equation by setting $\beta = z$. Consequently, the equation transforms into

$$S\frac{ds_\alpha}{dt} = \epsilon_{\alpha\gamma}\frac{dH}{ds_\gamma}, \tag{B17}$$

where now, α and γ are confined to x and y Cartesian directions. By reintroducing the matrix form and transferring the ϵ tensor to the left-hand side, we arrive at

$$-S\epsilon\frac{d\vec{s}}{dt} = \frac{dH}{d\vec{s}}. \tag{B18}$$

Referring back to Eq. (B6), it is noteworthy that $-S\epsilon$ is equivalent to the $G^{(\mathrm{ss})}$. Since the Hamiltonian has been expanded up to the quadratic order, the derivative $dH/d\vec{s}$ can be expressed as

$$\frac{dH}{d\vec{s}} = K^{(\mathrm{ss})}|s\rangle + K^{(\mathrm{sp})}|u\rangle, \tag{B19}$$

where we choose to use the bra-ket notation for ease of representation. This gives rise to

$$G^{(\mathrm{ss})}|\dot{s}\rangle = K^{(\mathrm{ss})}|s\rangle + K^{(\mathrm{sp})}|u\rangle, \tag{B20}$$

which aligns with the form presented in Eq. (B1). Thus, we have successfully shown the equivalence of the EOM for the spin-phonon model presented in this appendix with the undamped Landau-Lifshitz equation.

APPENDIX C: SPIN-SPIN HESSIANS ($K^{(ss)}$) AND BERRY CURVATURES ($\Omega^{(ss)}$) FOR ALL FOUR MATERIALS

In this appendix, we present the spin-spin Hessians and Berry curvatures for all four materials investigated in our study.

For bulk CrI_3, both the spin-spin Hessian ($K^{(ss)}$) and Berry curvature ($\Omega^{(ss)}$) matrices have the form

$$M_{4\times4} = \begin{pmatrix} a & b \\ b & a \end{pmatrix}, \tag{C1}$$

where both a and b are 2×2 matrices that are restricted to be of the form

$$a = a_{\mathrm{sym}}\begin{pmatrix} 1 & 0 \\ 0 & 1 \end{pmatrix} + a_{\mathrm{asym}}\begin{pmatrix} 0 & 1 \\ -1 & 0 \end{pmatrix}, \tag{C2}$$

and similarly for b, as a result of the threefold symmetry. In Table XI, we provide the symmetric and antisymmetric parts of a and b for both $K^{(ss)}$ and $\Omega^{(ss)}$ of bulk CrI_3. It is noteworthy that the eigenvalues of $\Omega^{(ss)}$ are 1.499 and 1.566 for the E_g and E_u modes, respectively. These values represent the effective spins of the respective magnon modes. They are close to $3/2$, as expected from the nominal spin of the Cr^{3+} ion, but they do differ slightly, especially for the optical E_u magnon. Instead, the deviation is very small for the acoustic E_g magnon. These deviations are not captured by the minimal spin-phonon model proposed in Ref. [33].

The symmetry-allowed matrix elements for monolayer CrI_3 exhibit a similar structure to those of bulk CrI_3, and they can also be decomposed following the same procedure as described in Eqs. (C1) and (C2). The numerical values of these matrix elements are provided in Table XI.

For bulk Cr_2O_3, the nonzero matrix elements of $K^{(ss)}$ are given by

$$K^{(ss)} = \begin{pmatrix} a & b & c & d \\ b^T & a^T & d & c^T \\ c^T & d^T & a & b^T \\ d^T & c & b & a^T \end{pmatrix}, \tag{C3}$$

while the nonzero matrix elements of $G^{(ss)}$ are

$$G^{(ss)} = \begin{pmatrix} a & b & c & d \\ -b^T & a^T & d & c^T \\ -c^T & -d^T & a & b^T \\ -d^T & -c & -b & a^T \end{pmatrix}. \tag{C4}$$

Here, a, b, c, and d can also be decomposed in the same manner as in Eq. (C2). The numerical results for these matrix elements are provided in Table XI.

For monolayer VPSe3, the matrix elements of both $K^{(ss)}$ and $\Omega^{(ss)}$ have the form

$$M_{4\times4} = \begin{pmatrix} a & b \\ b & a^T \end{pmatrix}, \tag{C5}$$

where a and b are 2×2 matrices. The values of these matrix elements can be found in Table XI.

From Table XI, we can find that, for the systems with at most two spins, the asymmetric (symmetric) parts of $K^{(ss)}$ ($G^{(ss)}$) all vanish. However, the symmetry is more complicated in Cr_2O_3, where some of the b, c, and d components in Eqs. (C3) and (C4) have both symmetric and asymmetric components.

TABLE XI. Matrix elements $K^{(ss)}$ and $\Omega^{(ss)}$ for materials under study (ML, monolayer). Symmetric ("sym") and antisymmetric ("asym") parts are defined in Eq. (C2). For $\Omega^{(ss)}$ of Cr_2O_3, the values of $c_{\mathrm{sym}} = -6.211\times10^{-5}$ and $d_{\mathrm{sym}} = -2.409\times10^{-4}$ appear rounded to zero.

		$K^{(ss)}$ (meV)		$\Omega^{(ss)}$	
Material	Term	Sym	Asym	Sym	Asym
CrI_3	a	18.340	0	0	−1.533
	b	−17.455	0	0	0.033
ML CrI_3	a	8.956	0	0	−1.526
	b	−7.497	0	0	0.026
Cr_2O_3	a	72.182	0	0	−1.454
	b	17.360	0.082	0	0
	c	−27.193	1.275	0.000	0.024
	d	27.479	0	0.000	0
ML $VPSe_3$	a	143.092	0	0	−1.351
	b	142.622	0	0	0

APPENDIX D: PERTURBATION TREATMENT OF PHONON-MAGNON DYNAMICS

In the main text, we directly solve the EOM of the present approach [Eq. (10)]. However, employing perturbation theory to solve the EOM can offer valuable physical insights into the influence of Hessian matrices and Berry curvatures on the results. In this section, we present a perturbation treatment for $K^{(sp)}$, $G^{(ps)}$, and $G^{(pp)}$ individually. Furthermore, we provide numerical results from the perturbation treatment of $K^{(sp)}$ and compare them with the predictions of the spin-phonon model.

We begin by reformulating Eq. (10) in matrix form as

$$(K + i\omega_i G - \omega_i^2 M)|q_i\rangle = 0, \tag{D1}$$

where the matrices M, K, and G are defined in Eq. (11). At variance with the main text, in this appendix we let i, j label mixed modes, while m, n and μ, ν label bare phonon and bare magnon modes, respectively. We utilize the bare phonon and magnon states $|u_n^{(0)}\rangle$ and $|s_\mu^{(0)}\rangle$ as the basis functions for the perturbation theory, where the superscript (0) denotes the zeroth order in the perturbation expansion.

The EOM for unperturbed phonons can be expressed in matrix form as

$$(K^{(\mathrm{pp})} - \xi_n M^{(\mathrm{pp})})|u_n^{(0)}\rangle = 0, \tag{D2}$$

where for convenience we introduce the squared frequency $\xi_n = \omega_n^2$, and for the magnons as

$$(K^{(\mathrm{ss})} + i\omega_\mu G^{(\mathrm{ss})})|s_\mu^{(0)}\rangle = 0, \tag{D3}$$

where ω_μ may be positive or negative even though solutions with negative energy are not physically observable. The fact that $\langle u_m^{(0)}|M^{(\mathrm{pp})}|u_n^{(0)}\rangle = 0$ for $\xi_m \neq \xi_n$ and that $\langle s_\mu^{(0)}|G^{(\mathrm{ss})}|s_\nu^{(0)}\rangle = 0$ for $\omega_\mu \neq \omega_\nu$ allows us to adopt the normalization conditions

$$\langle u_m^{(0)}|M^{(\mathrm{pp})}|u_n^{(0)}\rangle = \delta_{mn}, \tag{D4}$$

$$\langle s_\mu^{(0)}|iG^{(\mathrm{ss})}|s_\nu^{(0)}\rangle = \delta_{\mu\nu}\sigma_\mu, \tag{D5}$$

where σ_μ takes the values ∓ 1 for $\omega_\mu > 0$ and $\omega_\mu < 0$, respectively. The solution to Eq. (D1) is a composite vector that includes both the phonon and magnon sectors, living in the space spanned by basis vectors $|u_n^{(0)}\rangle \oplus |0\rangle$ and $|0\rangle \oplus |s_\mu^{(0)}\rangle$.

As discussed in the main text, phonons and magnons belonging to the E irreducible representations can be doubly degenerate. To address this, we need to employ degenerate perturbation theory. However, we can simplify the analysis by considering the $+$ and $-$ sectors separately. Phonons and magnons from different sectors do not mix, allowing us to work with these bases throughout this section.

1. Perturbation treatment of $K^{(\mathrm{sp})}$

We begin by examining the perturbation of $K^{(\mathrm{sp})}$ alone, neglecting $G^{(\mathrm{pp})}$ and $G^{(\mathrm{sp})}$. We replace $K^{(\mathrm{sp})}$ with $\lambda K^{(\mathrm{sp})}$, where λ serves as our perturbation parameter, and expand Eq. (D1) up to second order in λ as

$$\begin{aligned}
K &= K^{(0)} + \lambda K^{(1)},\\
K^{(0)} &= \begin{pmatrix} K^{(\mathrm{pp})} & 0 \\ 0 & K^{(\mathrm{ss})} \end{pmatrix},\\
K^{(1)} &= \begin{pmatrix} 0 & K^{(\mathrm{ps})} \\ K^{(\mathrm{sp})} & 0 \end{pmatrix},\\
\omega_i &= \omega_i^{(0)} + \lambda\omega_i^{(1)} + \lambda^2\omega_i^{(2)} + \ldots,\\
\xi_i &= \xi_i^{(0)} + \lambda\xi_i^{(1)} + \lambda^2\xi_i^{(2)} + \ldots,\\
|q_i\rangle &= |q_i^{(0)}\rangle + \lambda|q_i^{(1)}\rangle + \lambda^2|q_i^{(2)}\rangle + \ldots.
\end{aligned} \tag{D6}$$

We substitute these equations into Eq. (D1) and expand in orders of λ, making use of the relations

$$\begin{aligned}
\xi_i^{(0)} &= (\omega_i^{(0)})^2,\\
\xi_i^{(1)} &= 2\omega_i^{(0)}\omega_i^{(1)},\\
\xi_i^{(2)} &= (\omega_i^{(1)})^2 + 2\omega_i^{(0)}\omega_i^{(2)}.
\end{aligned} \tag{D7}$$

At zero order, this yields

$$(K^{(0)} + i\omega_i^{(0)}G - \xi_i^{(0)}M)|q_i^{(0)}\rangle = 0, \tag{D8}$$

which corresponds to the EOM for decoupled phonons and magnons.

The equation at first order in λ is

$$\begin{aligned}
&(K^{(0)} + i\omega_i^{(0)}G - \xi_i^{(0)}M)|q_i^{(1)}\rangle\\
&\quad + (K^{(1)} + i\omega_i^{(1)}G - \xi_i^{(1)}M)|q_i^{(0)}\rangle = 0.
\end{aligned} \tag{D9}$$

Multiplying Eq. (D9) on the left by $\langle q_i^{(0)}|$, noting that $\langle q_i^{(0)}|(K^{(0)} + i\omega_i^{(0)}G - \xi_i^{(0)}M) = 0$, and also that $\langle q_i^{(0)}|K^{(1)}|q_i^{(0)}\rangle = 0$ since $K^{(1)}$ is block off diagonal in the phonon and magnon d.o.f., we obtain

$$\omega_i^{(1)}(\langle q_i^{(0)}|iG|q_i^{(0)}\rangle - 2\omega_i^0\langle q_i^{(0)}|M|q_i^{(0)}\rangle) = 0, \tag{D10}$$

which indicates that $\omega_i^{(1)} = 0$, so that also $\xi_i^{(1)} = 0$. This is similar to the perturbation theory in quantum mechanics, where the first-order energy correction is always given by the diagonal matrix element of the interaction Hamiltonian, which is zero in our case.

To obtain $|q_i^{(1)}\rangle$, we multiply Eq. (D9) by $\langle q_j^{(0)}|$ on the left and use $\omega_i^{(1)} = \xi_i^{(1)} = 0$. This gives

$$\langle q_j^{(0)}|K^{(0)} + i\omega_i^{(0)}G - \xi_i^{(0)}M|q_i^{(1)}\rangle + \langle q_j^{(0)}|K^{(1)}|q_i^{(0)}\rangle = 0. \tag{D11}$$

We observe that if i and j both label phonons or both label magnons, $K^{(1)}$ has no effect. Therefore, $|q_n^{(1)}\rangle$ for phonons

has a pure magnon character, and $|q_\mu^{(1)}\rangle$ for magnons has a pure phonon character.

a. Perturbation of phonons

We focus on the perturbation for phonons first, and we replace $|q_i\rangle$ and $|q_j\rangle$ in Eq. (D11) with $|u_n\rangle$ and $|s_\mu\rangle$, respectively. Then, Eq. (D11) becomes

$$\langle s_\mu^{(0)}|K^{(0)}+i\omega_n^{(0)}G-\xi_n^{(0)}M|u_n^{(1)}\rangle+\langle s_\mu^{(0)}|K^{(\mathrm{sp})}|u_n^{(0)}\rangle=0. \tag{D12}$$

To obtain $|u_n^{(1)}\rangle$, we expand it in terms of the basis $|s_\nu^{(0)}\rangle$ as

$$|u_n^{(1)}\rangle=\sum_\nu c_{\nu n}^{(1)}|s_\nu^{(0)}\rangle. \tag{D13}$$

Substituting Eq. (D13) into Eq. (D12), we have

$$\sum_\nu c_{\nu n}^{(1)}\langle s_\mu^{(0)}|K^{(\mathrm{ss})}+i\omega_n^{(0)}G^{(\mathrm{ss})}|s_\nu^{(0)}\rangle+\langle s_\mu^{(0)}|K^{(\mathrm{sp})}|u_n^{(0)}\rangle=0. \tag{D14}$$

Using the relation $(K^{(\mathrm{ss})}+i\omega_\nu^{(0)}G^{(\mathrm{ss})})|s_\nu^{(0)}\rangle=0$, we find

$$\begin{aligned}\sum_\nu c_{\nu n}^{(1)}\omega_{n\nu}^{(0)}\langle s_\mu^{(0)}|iG^{(\mathrm{ss})}|s_\nu^{(0)}\rangle+\langle s_\mu^{(0)}|K^{(\mathrm{sp})}|u_n^{(0)}\rangle\\ =c_{\mu n}^{(1)}\omega_{n\mu}^{(0)}\sigma_\mu+\langle s_\mu^{(0)}|K^{(\mathrm{sp})}|u_n^{(0)}\rangle=0,\end{aligned} \tag{D15}$$

where $\omega_{n\mu}^{(0)}$ denotes $\omega_n^{(0)}-\omega_\mu^{(0)}$. Using Eq. (D15), we can determine $c_{\mu n}^{(1)}$ and express $|u_n^{(1)}\rangle$ as

$$|u_n^{(1)}\rangle=\sum_\mu\sigma_\mu\frac{\langle s_\mu^{(0)}|K^{(\mathrm{sp})}|u_n^{(0)}\rangle}{\omega_\mu^{(0)}-\omega_n^{(0)}}|s_\mu^{(0)}\rangle. \tag{D16}$$

This is the first major result of this appendix. It is worth noting that the first-order perturbation of the phonons has only spin character, so that the phonon character remains unchanged. This cannot explain why the angular momentum summed over a pair of E_g or E_u chiral phonons is not zero, as can be seen in Tables I and VIII of the main text. To explain this effect, we need to consider the second-order perturbation.

Since we have seen that the first-order correction $\omega_n^{(1)}$ to the phonon energy vanishes, we need to calculate the second-order correction $\omega_n^{(2)}$ in order to determine the energy splitting of the chiral phonons. By expanding Eq. (D1) to the second order in λ, we obtain

$$\begin{aligned}(K^{(0)}+i\omega_i^{(0)}G-\xi_i^{(0)}M)|q_i^{(2)}\rangle+K^{(1)}|q_i^{(1)}\rangle\\ +(i\omega_i^{(2)}G-\xi_i^{(2)}M)|q_i^{(0)}\rangle=0.\end{aligned} \tag{D17}$$

Multiplying Eq. (D17) by $\langle q_i^{(0)}|$ from the left, we obtain

$$\langle q_i^{(0)}|K^{(1)}|q_i^{(1)}\rangle+\langle q_i^{(0)}|i\omega_i^{(2)}G-\xi_i^{(2)}M|q_i^{(0)}\rangle=0. \tag{D18}$$

For phonons, we replace $|q_i\rangle$ with $|u_n\rangle$ and substitute Eq. (D16) into Eq. (D18), yielding

$$\xi_n^{(2)}=\sum_\mu\sigma_\mu\frac{|\langle s_\mu^{(0)}|K^{(\mathrm{sp})}|u_n^{(0)}\rangle|^2}{\omega_\mu^{(0)}-\omega_n^{(0)}}, \tag{D19}$$

or equivalently,

$$\omega_n^{(2)}=\sum_\mu\sigma_\mu\frac{|\langle s_\mu^{(0)}|K^{(\mathrm{sp})}|u_n^{(0)}\rangle|^2}{2\omega_n^{(0)}(\omega_\mu^{(0)}-\omega_n^{(0)})}. \tag{D20}$$

This is a second major result. The summation over μ in Eqs. (D16) and (D20) runs over all solutions of Eq. (D3), including those of negative energy. Thus, the unphysical negative-energy states can still contribute to the perturbation of the phonons. It is worth noting that Eq. (D20) explains why phonons from the + sector exhibit larger energy splitting. Since positive-energy magnons also belong to the + sector, the interactions between magnons and phonons are stronger in the + sector due to the smaller energy denominator.

Furthermore, we can obtain $|u_n^{(2)}\rangle$ by left-multiplying Eq. (D17) with $\langle q_j^{(0)}|$. This yields

$$\begin{aligned}\langle q_j^{(0)}|K^{(0)}+i\omega_i^{(0)}G-\xi_i^{(0)}M|q_i^{(2)}\rangle+\langle q_j^{(0)}|K^{(1)}|q_i^{(1)}\rangle\\ +\langle q_j^{(0)}|i\omega_i^{(2)}G-\xi_i^{(2)}M|q_i^{(0)}\rangle=0.\end{aligned} \tag{D21}$$

If i labels a phonon and j labels a magnon, both the second and third terms in Eq. (D21) are zero, implying that the first term is also zero. It follows that $|q_i^{(2)}\rangle$ can possess only phonon character. Replacing $|q_i\rangle$ and $|q_j\rangle$ by $|u_n\rangle$ and $|u_m\rangle$ and substituting Eq. (D16) into Eq. (D21) yields

$$|u_n^{(2)}\rangle=\sum_{m\neq n}\sum_\mu\sigma_\mu\frac{\langle u_m^{(0)}|K^{(\mathrm{ps})}|s_\mu^{(0)}\rangle\langle s_\mu^{(0)}|K^{(\mathrm{sp})}|u_n^{(0)}\rangle}{(\xi_n^{(0)}-\xi_m^{(0)})(\omega_\mu^{(0)}-\omega_n^{(0)})}|u_m^{(0)}\rangle, \tag{D22}$$

which represents the effect of the magnon-mediated phonon-phonon interaction at second order. It provides an explanation for the noncanceling angular momentum observed in chiral phonon pairs, as shown in Tables I and VIII.

b. Perturbation of magnons

We now turn to the corresponding perturbation treatment of the magnons. First, we replace $|q_i\rangle$ and $|q_j\rangle$ in Eq. (D11)

with $|s_\mu\rangle$ and $|u_n\rangle$, respectively. Then, we multiply Eq. (D11) by $|u_n^{(0)}\rangle$ from the left, resulting in

$$\langle u_n^{(0)}|K^{(0)} + i\omega_\mu^{(0)} G - \xi_\mu^{(0)} M|s_\mu^{(1)}\rangle + \langle u_n^{(0)}|K^{(\mathrm{ps})}|s_\mu^{(0)}\rangle = 0. \tag{D23}$$

Next, we expand $|s_\mu^{(1)}\rangle$ in terms of the basis of $|u_m^{(0)}\rangle$ as

$$|s_\mu^{(1)}\rangle = \sum_m d_{m\mu}^{(1)}|u_m^{(0)}\rangle. \tag{D24}$$

Substituting this expansion into Eq. (D23), we obtain

$$\sum_m d_{m\mu}^{(1)}\langle u_n^{(0)}|K^{(\mathrm{pp})} - \xi_\mu^{(0)} M|u_m^{(0)}\rangle + \langle u_n^{(0)}|K^{(\mathrm{ps})}|s_\mu^{(0)}\rangle = -d_{n\mu}^{(1)}\xi_{\mu n} + \langle u_n^{(0)}|K^{(\mathrm{ps})}|s_\mu^{(0)}\rangle = 0. \tag{D25}$$

From Eq. (D25), we can determine the coefficients $d_{n\mu}^{(1)}$. Therefore, the first-order perturbation of the magnons is given by

$$|s_\mu^{(1)}\rangle = \sum_n \frac{\langle u_n^{(0)}|K^{(\mathrm{ps})}|s_\mu^{(0)}\rangle}{\xi_\mu^{(0)} - \xi_n^{(0)}}|u_n^{(0)}\rangle. \tag{D26}$$

To get the second-order energy perturbation for magnons, we replace $|q_i\rangle$ with $|s_\mu\rangle$ and substitute Eq. (D26) into Eq. (D18). This leads to

$$\omega_\mu^{(2)} = \sum_n \sigma_\mu \frac{|\langle u_n^{(0)}|K^{(\mathrm{ps})}|s_\mu^{(0)}\rangle|^2}{\xi_n^{(0)} - \xi_\mu^{(0)}}. \tag{D27}$$

The second-order perturbation of the magnon states can be obtained in a way similar to what was done for the phonons. We replace $|q_i\rangle$ and $|q_j\rangle$ with $|s_\mu\rangle$ and $|s_\nu\rangle$ and substitute Eq. (D26) into Eq. (D21). This substitution yields

$$|s_\mu^{(2)}\rangle = \sum_{\nu\neq\mu}\sum_n \sigma_\nu \frac{\langle s_\nu^{(0)}|K^{(\mathrm{sp})}|u_n^{(0)}\rangle\langle u_n^{(0)}|K^{(\mathrm{ps})}|s_\mu^{(0)}\rangle}{(\omega_\mu^{(0)} - \omega_\nu^{(0)})(\xi_n^{(0)} - \xi_\mu^{(0)})}|s_\nu^{(0)}\rangle. \tag{D28}$$

We are now prepared to present the numerical results obtained using the perturbation approach. The neglect of $G^{(\mathrm{sp})}$ and $G^{(\mathrm{pp})}$ corresponds to the spin-phonon model presented in Appendix B, which can be solved exactly. Consequently, we can utilize the exact solution as a benchmark to evaluate the accuracy of the perturbation approach, and we choose bulk CrI_3 as the benchmark system. In Table XII, we provide several quantities calculated using perturbed energies and states. These include the second-order-perturbed phonon energies, the first-order-perturbed phonon states represented by the coefficients $c_{\nu n}^{(1)}$ defined in Eq. (D13), and the second-order-perturbed magnon energies. The corresponding exact results are also included in Table XII for benchmarking purposes, and we find that the perturbation treatment reproduces the exact solutions to very good accuracy. We perform calculations of the angular momentum L_z using the second-order-perturbed phonon states, and the values obtained agree with the numbers presented in Table I up to the fourth decimal place. As a result, we do not include the specific numerical results for L_z explicitly in the table.

TABLE XII. Comparison of perturbation approach and exact solution in the spin-phonon model. The perturbation approach provides second-order perturbations to phonon and magnon energies $E_n^{(2)} = \hbar\omega_n^{(2)}$ and first-order perturbations to phonon states $c_{\nu n}^{(1)}$. The exact solutions for phonon and magnon energy shifts $\Delta E = \hbar\Delta\omega$ and the spin component of phononlike solutions $c_{\nu n}$ are included as benchmarks. The bare phonon and magnon energies $E_n^{(0)} = \hbar\omega_n^{(0)}$ are provided as reference values for energy perturbations or shifts.

Irrep	$E_n^{(0)}$ (meV)	$E_n^{(2)}$ (μeV)	ΔE (μeV)	$c_{\nu n}^{(1)}$ (10^{-3})	$c_{\nu n}$ (10^{-3})
Phonons					
E_g	7.000	−1.323	−1.324	1.562	1.563
		1.566	1.565	1.850	1.849
	12.929	−0.545	−0.545	1.021	1.021
		0.597	0.597	1.118	1.118
	13.488	−0.244	−0.244	0.684	0.683
		0.266	0.266	0.746	0.747
	29.852	−0.001	−0.001	0.050	0.050
		0.001	0.001	0.052	0.052
E_u	10.769	−4.431	−4.453	2.809	2.823
		−1.593	−1.597	1.010	1.012
	14.329	−17.563	−17.546	7.680	7.668
		−4.030	−4.031	1.762	1.763
	27.823	−3.506	−3.506	1.962	1.962
		35.836	35.623	20.053	19.947
Magnons					
E_g	0.590	−4.544	−4.543		
E_u	22.864	−22.971	−22.757		

2. Perturbation treatment of $G^{(\mathrm{sp})}$

The treatment of $G^{(\mathrm{sp})}$ in the perturbation framework follows a similar procedure to that of $K^{(\mathrm{sp})}$. In this case, we neglect $K^{(\mathrm{sp})}$ and $G^{(\mathrm{pp})}$. Since $G^{(\mathrm{sp})}$ is block off diagonal, the first-order perturbation of the energy is also zero. By substituting $K^{(\mathrm{sp})}$ with $i\omega_n G^{(\mathrm{sp})}$ in Eq. (D16), we can obtain $|u_n^{(1)}\rangle$ due to $G^{(\mathrm{sp})}$. Similarly, perturbations $\omega_n^{(2)}$ and $|u_n^{(2)}\rangle$ due to $G^{(\mathrm{sp})}$ can be obtained by replacing $K^{(\mathrm{sp})}$ with $i\omega_n G^{(\mathrm{sp})}$ in Eqs. (D20) and (D22), respectively. Perturbations of magnons can be obtained in the same manner.

3. Perturbation treatment of $G^{(\mathrm{pp})}$

In this section, we explore the perturbation treatment of $G^{(\mathrm{pp})}$, this time neglecting $K^{(\mathrm{sp})}$ and $G^{(\mathrm{sp})}$. Taking the perturbation to be $\lambda G^{(\mathrm{pp})}$, Eq. (D1) simplifies to

$$(K^{(\mathrm{pp})} + i\omega_n G^{(\mathrm{pp})} - \xi_n M^{(\mathrm{pp})})|u_n\rangle = 0. \tag{D29}$$

We expand each term as

$$\begin{aligned}\omega_n &= \omega_n^{(0)} + \lambda\omega_n^{(1)} + \lambda^2\omega_n^{(2)} + \ldots,\\ \xi_n &= \xi_n^{(0)} + \lambda\xi_n^{(1)} + \lambda^2\xi_n^{(2)} + \ldots,\\ |u_n\rangle &= |u_n^{(0)}\rangle + \lambda|u_n^{(1)}\rangle + \lambda^2|u_n^{(2)}\rangle + \ldots,\end{aligned} \tag{D30}$$

where $K^{(\mathrm{pp})}$ and $M^{(\mathrm{pp})}$ are of zeroth order in λ, and $G^{(\mathrm{pp})}$ is of first order in λ.

Expanding Eq. (D29) to the first order in λ, we obtain

$$\begin{aligned}&(K^{(\mathrm{pp})} - \xi_n^{(0)} M^{(\mathrm{pp})})|u_n^{(1)}\rangle\\ &\quad + (i\omega_n^{(0)} G^{(\mathrm{pp})} - \xi_n^{(1)} M^{(\mathrm{pp})})|u_n^{(0)}\rangle = 0.\end{aligned} \tag{D31}$$

Multiplying Eq. (D31) by $\langle u_n^{(0)}|$ from the left, we find the first-order perturbation to the phonon energy as

$$\begin{aligned}\xi_n^{(1)} &= \omega_n^{(0)}\langle u_n^{(0)}|iG^{(\mathrm{pp})}|u_n^{(0)}\rangle,\\ \omega_n^{(1)} &= \frac{1}{2}\langle u_n^{(0)}|iG^{(\mathrm{pp})}|u_n^{(0)}\rangle.\end{aligned} \tag{D32}$$

Multiplying Eq. (D31) by $\langle u_m^{(0)}|$ from the left, we obtain the first-order perturbation to $|u_n\rangle$ as

$$|u_n^{(1)}\rangle = \sum_{m\neq n} \frac{i\omega_n\langle u_m^{(0)}|G^{(\mathrm{pp})}|u_n^{(0)}\rangle}{\xi_n^{(0)} - \xi_m^{(0)}}|u_m^{(0)}\rangle. \tag{D33}$$

Since the first-order perturbations to energies and phonon states are nonzero in this case, we do not go beyond first order here, although generalizing to higher orders is straightforward.

[1] Xavier Gonze and Changyol Lee, *Dynamical matrices, Born effective charges, dielectric permittivity tensors, and interatomic force constants from density-functional perturbation theory*, Phys. Rev. B **55**, 10355 (1997).

[2] Stefano Baroni, Stefano de Gironcoli, Andrea Dal Corso, and Paolo Giannozzi, *Phonons and related crystal properties from density-functional perturbation theory*, Rev. Mod. Phys. **73**, 515 (2001).

[3] Atsushi Togo, Laurent Chaput, Terumasa Tadano, and Isao Tanaka, *Implementation strategies in* PHONOPY *and* PHONO3PY, J. Phys. Condens. Matter **35**, 353001 (2023).

[4] Feliciano Giustino, *Electron-phonon interactions from first principles*, Rev. Mod. Phys. **89**, 015003 (2017).

[5] Bartomeu Monserrat, *Electron-phonon coupling from finite differences*, J. Phys. Condens. Matter **30**, 083001 (2018).

[6] A. I. Liechtenstein, M. I. Katsnelson, V. P. Antropov, and V. A. Gubanov, *Local spin density functional approach to the theory of exchange interactions in ferromagnetic metals and alloys*, J. Magn. Magn. Mater. **67**, 65 (1987).

[7] S. V. Halilov, H. Eschrig, A. Y. Perlov, and P. M. Oppeneer, *Adiabatic spin dynamics from spin-density-functional theory: Application to* Fe, Co, *and* Ni, Phys. Rev. B **58**, 293 (1998).

[8] Liqin Ke and Mikhail I. Katsnelson, *Electron correlation effects on exchange interactions and spin excitations in 2d van der Waals materials*, npj Comput. Mater. **7**, 4 (2021).

[9] Frederik L. Durhuus, Thorbjørn Skovhus, and Thomas Olsen, *Plane wave implementation of the magnetic force theorem for magnetic exchange constants: application to bulk* Fe, Co, *and* Ni, J. Phys. Condens. Matter **35**, 105802 (2023).

[10] S. Y. Savrasov, *Linear response calculations of spin fluctuations*, Phys. Rev. Lett. **81**, 2570 (1998).

[11] S. Lounis, A. T. Costa, R. B. Muniz, and D. L. Mills, *Theory of local dynamical magnetic susceptibilities from the Korringa-Kohn-Rostoker Green function method*, Phys. Rev. B **83**, 035109 (2011).

[12] Bruno Rousseau, Asier Eiguren, and Aitor Bergara, *Efficient computation of magnon dispersions within time-dependent density functional theory using maximally localized Wannier functions*, Phys. Rev. B **85**, 054305 (2012).

[13] A. L. Wysocki, V. N. Valmispild, A. Kutepov, S. Sharma, J. K. Dewhurst, E. K. U. Gross, A. I. Lichtenstein, and V. P. Antropov, *Spin-density fluctuations and the fluctuation-dissipation theorem in 3d ferromagnetic metals*, Phys. Rev. B **96**, 184418 (2017).

[14] Kun Cao, Henry Lambert, Paolo G. Radaelli, and Feliciano Giustino, *Ab initio calculation of spin fluctuation spectra using time-dependent density functional perturbation theory, plane waves, and pseudopotentials*, Phys. Rev. B **97**, 024420 (2018).

[15] N. Tancogne-Dejean, F. G. Eich, and A. Rubio, *Time-dependent magnons from first principles*, J. Chem. Theory Comput. **16**, 1007 (2020).

[16] Thorbjørn Skovhus and Thomas Olsen, *Dynamic transverse magnetic susceptibility in the projector augmented-wave method: Application to* Fe, Ni, *and*, Co, Phys. Rev. B **103**, 245110 (2021).

[17] Tommaso Gorni, Oscar Baseggio, Pietro Delugas, Stefano Baroni, and Iurii Timrov, TURBOMAGNON*—a code for the simulation of spin-wave spectra using the Liouville-Lanczos approach to time-dependent density-functional perturbation theory*, Comput. Phys. Commun. **280**, 108500 (2022).

[18] F. Aryasetiawan and K. Karlsson, *Green's function formalism for calculating spin-wave spectra*, Phys. Rev. B **60**, 7419 (1999).

[19] K. Karlsson and F. Aryasetiawan, *Spin-wave excitation spectra of nickel and iron*, Phys. Rev. B **62**, 3006 (2000).

[20] Takao Kotani and Mark van Schilfgaarde, *Spin wave dispersion based on the quasiparticle self-consistent GW*

method: NiO, MnO *and* α-MnAs, J. Phys. Condens. Matter **20**, 295214 (2008).
[21] Ersoy Şaşıoğlu, Arno Schindlmayr, Christoph Friedrich, Frank Freimuth, and Stefan Blügel, *Wannier-function approach to spin excitations in solids*, Phys. Rev. B **81**, 054434 (2010).
[22] Mathias C. T. D. Müller, Stefan Blügel, and Christoph Friedrich, *Electron-magnon scattering in elementary ferromagnets from first principles: Lifetime broadening and band anomalies*, Phys. Rev. B **100**, 045130 (2019).
[23] Pietro Delugas, Oscar Baseggio, Iurii Timrov, Stefano Baroni, and Tommaso Gorni, *Magnon-phonon interactions enhance the gap at the Dirac point in the spin-wave spectra of* CrI_3 *two-dimensional magnets*, Phys. Rev. B **107**, 214452 (2023).
[24] Max Born and Kun Huang, *Dynamical Theory of Crystal Lattices*, International Series of Monographs on Physics (Oxford University Press, Oxford, 1954).
[25] C. Alden Mead and Donald G. Truhlar, *On the determination of Born-Oppenheimer nuclear motion wave functions including complications due to conical intersections and identical nuclei*, J. Chem. Phys. **70**, 2284 (1979).
[26] Lifa Zhang and Qian Niu, *Angular momentum of phonons and the Einstein–de Haas effect*, Phys. Rev. Lett. **112**, 085503 (2014).
[27] Hao Chen, Wei Zhang, Qian Niu, and Lifa Zhang, *Chiral phonons in two-dimensional materials*, 2D Mater. **6**, 012002 (2018).
[28] Sinisa Coh, *Classification of materials with phonon angular momentum and microscopic origin of angular momentum*, Phys. Rev. B **108**, 134307 (2023).
[29] Hisayoshi Komiyama and Shuichi Murakami, *Universal features of canonical phonon angular momentum without time-reversal symmetry*, Phys. Rev. B **103**, 214302 (2021).
[30] Oliviero Bistoni, Francesco Mauri, and Matteo Calandra, *Intrinsic vibrational angular momentum from nonadiabatic effects in noncollinear magnetic molecules*, Phys. Rev. Lett. **126**, 225703 (2021).
[31] Daniyar Saparov, Bangguo Xiong, Yafei Ren, and Qian Niu, *Lattice dynamics with molecular Berry curvature: Chiral optical phonons*, Phys. Rev. B **105**, 064303 (2022).
[32] Qianqian Wang, Si Li, Jiaojiao Zhu, Hao Chen, Weikang Wu, Weibo Gao, Lifa Zhang, and Shengyuan A. Yang, *Chiral phonons in lattices with* C_4 *symmetry*, Phys. Rev. B **105**, 104301 (2022).
[33] John Bonini, Shang Ren, David Vanderbilt, Massimiliano Stengel, Cyrus E. Dreyer, and Sinisa Coh, *Frequency splitting of chiral phonons from broken time-reversal symmetry in* CrI_3, Phys. Rev. Lett. **130**, 086701 (2023).
[34] Lifa Zhang, Jie Ren, Jian-Sheng Wang, and Baowen Li, *Topological nature of the phonon Hall effect*, Phys. Rev. Lett. **105**, 225901 (2010).
[35] Tao Qin, Jianhui Zhou, and Junren Shi, *Berry curvature and the phonon Hall effect*, Phys. Rev. B **86**, 104305 (2012).
[36] Lifa Zhang, *Berry curvature and various thermal Hall effects*, New J. Phys. **18**, 103039 (2016).
[37] Takuma Saito, Kou Misaki, Hiroaki Ishizuka, and Naoto Nagaosa, *Berry phase of phonons and thermal Hall effect in nonmagnetic insulators*, Phys. Rev. Lett. **123**, 255901 (2019).
[38] Luojun Du, Jian Tang, Yanchong Zhao, Xiaomei Li, Rong Yang, Xuerong Hu, Xueyin Bai, Xiao Wang, Kenji Watanabe, Takashi Taniguchi, Dongxia Shi, Guoqiang Yu, Xuedong Bai, Tawfique Hasan, Guangyu Zhang, and Zhipei Sun, *Lattice dynamics, phonon chirality, and spin-phonon coupling in 2D itinerant ferromagnet* Fe_3GeTe_2, Adv. Funct. Mater. **29**, 1904734 (2019).
[39] Tingting Yin, Kanchan Ajit Ulman, Sheng Liu, Andrés Granados del Águila, Yuqing Huang, Lifa Zhang, Marco Serra, David Sedmidubsky, Zdenek Sofer, Su Ying Quek, and Qihua Xiong, *Chiral phonons and giant magneto-optical effect in* $CrBr_3$ *2D magnet*, Adv. Mater. **33**, 2101618 (2021).
[40] G. Grissonnanche, A. Legros, S. Badoux, E. Lefrançois, V. Zatko, M. Lizaire, F. Laliberté, A. Gourgout, J. S. Zhou, S. Pyon, T. Takayama, H. Takagi, S. Ono, N. Doiron-Leyraud, and L. Taillefer, *Giant thermal Hall conductivity in the pseudogap phase of cuprate superconductors*, Nature (London) **571**, 376 (2019).
[41] Heda Zhang, Chunqiang Xu, Caitlin Carnahan, Milos Sretenovic, Nishchay Suri, Di Xiao, and Xianglin Ke, *Anomalous thermal Hall effect in an insulating van der Waals magnet*, Phys. Rev. Lett. **127**, 247202 (2021).
[42] Shao-Yu Chen, Changxi Zheng, Michael S. Fuhrer, and Jun Yan, *Helicity-resolved Raman scattering of* MoS_2, $MoSe_2$, WS_2, *and* WSe_2 *atomic layers*, Nano Lett. **15**, 2526 (2015).
[43] Xiaotong Chen, Xin Lu, Sudipta Dubey, Qiang Yao, Sheng Liu, Xingzhi Wang, Qihua Xiong, Lifa Zhang, and Ajit Srivastava, *Entanglement of single-photons and chiral phonons in atomically thin* WSe_2, Nat. Phys. **15**, 221 (2019).
[44] Hanyu Zhu, Jun Yi, Ming-Yang Li, Jun Xiao, Lifa Zhang, Chih-Wen Yang, Robert A. Kaindl, Lain-Jong Li, Yuan Wang, and Xiang Zhang, *Observation of chiral phonons*, Science **359**, 579 (2018).
[45] Lifa Zhang and Qian Niu, *Chiral phonons at high-symmetry points in monolayer hexagonal lattices*, Phys. Rev. Lett. **115**, 115502 (2015).
[46] Hannes Hübener, Umberto De Giovannini, and Angel Rubio, *Phonon driven Floquet matter*, Nano Lett. **18**, 1535 (2018).
[47] Yafei Ren, Cong Xiao, Daniyar Saparov, and Qian Niu, *Phonon magnetic moment from electronic topological magnetization*, Phys. Rev. Lett. **127**, 186403 (2021).
[48] Dominik M. Juraschek, Tomáš Neuman, and Prineha Narang, *Giant effective magnetic fields from optically driven chiral phonons in* $4f$ *paramagnets*, Phys. Rev. Res. **4**, 013129 (2022).
[49] Xiao-Wei Zhang, Yafei Ren, Chong Wang, Ting Cao, and Di Xiao, *Gate-tunable phonon magnetic moment in bilayer graphene*, Phys. Rev. Lett. **130**, 226302 (2023).
[50] Qian Niu and Leonard Kleinman, *Spin-wave dynamics in real crystals*, Phys. Rev. Lett. **80**, 2205 (1998).
[51] Ralph Gebauer and Stefano Baroni, *Magnons in real materials from density-functional theory*, Phys. Rev. B **61**, R6459 (2000).
[52] Lev Davidovich Landau and E Lifshitz, *On the theory of the dispersion of magnetic permeability in ferromagnetic*

bodies, Phys. Z. Sowjetunion **8**, 153 (1935), https://cds.cern.ch/record/437299.

[53] Q. Niu, Xindong Wang, L. Kleinman, Wu-Ming Liu, D. M. C. Nicholson, and G. M. Stocks, *Adiabatic dynamics of local spin moments in itinerant magnets*, Phys. Rev. Lett. **83**, 207 (1999).

[54] We are aware that in some literature, the PAM is referred to as "pseudo angular momentum" [45], which is a nonzero integer multiple of $\hbar$ if the phonon respects C_n symmetry with a nontrivial eigenvalue. However, it is important to note that the phonon angular momentum discussed in this paper is the kinetic angular momentum and is not conserved in the absence of infinitesimal rotational symmetry in the lattice. In contrast, the pseudo angular momentum is conserved up to $n\hbar$ if the system possesses C_n symmetry. In Sec. IV, we refer to the C_3 eigenvalue as $\chi(C_3)$.

[55] David Vanderbilt, *Berry Phases in Electronic Structure Theory: Electric Polarization, Orbital Magnetization and Topological Insulators* (Cambridge University Press, Cambridge, England, 2018), Chap. 3.

[56] G. Kresse and J. Hafner, *Ab initio molecular dynamics for liquid metals*, Phys. Rev. B **47**, 558 (1993).

[57] G. Kresse and J. Furthmüller, *Efficient iterative schemes for ab initio total-energy calculations using a plane-wave basis set*, Phys. Rev. B **54**, 11169 (1996).

[58] G. Kresse and D. Joubert, *From ultrasoft pseudopotentials to the projector augmented-wave method*, Phys. Rev. B **59**, 1758 (1999).

[59] J. P. Perdew and Alex Zunger, *Self-interaction correction to density-functional approximations for many-electron systems*, Phys. Rev. B **23**, 5048 (1981).

[60] P. E. Blöchl, *Projector augmented-wave method*, Phys. Rev. B **50**, 17953 (1994).

[61] Hendrik J. Monkhorst and James D. Pack, *Special points for Brillouin-zone integrations*, Phys. Rev. B **13**, 5188 (1976).

[62] S. L. Dudarev, G. A. Botton, S. Y. Savrasov, C. J. Humphreys, and A. P. Sutton, *Electron-energy-loss spectra and the structural stability of nickel oxide: An* LSDA + U *study*, Phys. Rev. B **57**, 1505 (1998).

[63] Sai Mu and K. D. Belashchenko, *Influence of strain and chemical substitution on the magnetic anisotropy of antiferromagnetic* Cr_2O_3*: An ab-initio study*, Phys. Rev. Mater. **3**, 034405 (2019).

[64] Bheema Lingam Chittari, Youngju Park, Dongkyu Lee, Moonsup Han, Allan H. MacDonald, Euyheon Hwang, and Jeil Jung, *Electronic and magnetic properties of single-layer* MPX_3 *metal phosphorous trichalcogenides*, Phys. Rev. B **94**, 184428 (2016).

[65] Mark E. Turiansky, Audrius Alkauskas, Manuel Engel, Georg Kresse, Darshana Wickramaratne, Jimmy-Xuan Shen, Cyrus E. Dreyer, and Chris G. Van de Walle, *Nonrad: Computing nonradiative capture coefficients from first principles*, Comput. Phys. Commun. **267**, 108056 (2021).

[66] Harold T. Stokes and Dorian M. Hatch, *FINDSYM: Program for identifying the space-group symmetry of a crystal*, J. Appl. Crystallogr. **38**, 237 (2005).

[67] Atsushi Togo and Isao Tanaka, *SPGLIB: A software library for crystal symmetry search*, arXiv:1808.01590.

[68] Koichi Momma and Fujio Izumi, *VESTA3 for three-dimensional visualization of crystal, volumetric and morphology data*, J. Appl. Crystallogr. **44**, 1272 (2011).

[69] Bevin Huang, Genevieve Clark, Efrén Navarro-Moratalla, Dahlia R. Klein, Ran Cheng, Kyle L. Seyler, Ding Zhong, Emma Schmidgall, Michael A. McGuire, David H. Cobden, Wang Yao, Di Xiao, Pablo Jarillo-Herrero, and Xiaodong Xu, *Layer-dependent ferromagnetism in a van der Waals crystal down to the monolayer limit*, Nature (London) **546**, 270 (2017).

[70] Mildred S. Dresselhaus, Gene Dresselhaus, and Ado Jorio, *Group Theory: Application to the Physics of Condensed Matter* (Springer Science & Business Media, New York, 2007).

[71] The results presented in Table I for the spin-phonon model differ from those in Ref. [33] because in this paper, all matrices are calculated using DFT, while in Ref. [33], experimental magnon energies are used to evaluate $K^{(\mathrm{ss})}$, and the approximation in Eq. (B6) is taken.

[72] It is important to clarify that the reference to the clockwise rotation of the two spins is in the context of their motion as viewed from the direction of s_z. However, viewed from the direction of M_z, which is opposite to s_z, the two magnetic moments still rotate counterclockwise in the (M_x, M_y) plane.

[73] Shangfei Wu, Kai Du, Sang-Wook Cheong, and Girsh Blumberg (unpublished).

[74] Mois Ilia Aroyo, Juan Manuel Perez-Mato, Cesar Capillas, Eli Kroumova, Svetoslav Ivantchev, Gotzon Madariaga, Asen Kirov, and Hans Wondratschek, *Bilbao Crystallographic Server: I. Databases and crystallographic computing programs*, Z. Kristallogr. **221**, 15 (2006).

[75] Mois I. Aroyo, Asen Kirov, Cesar Capillas, J. M. Perez-Mato, and Hans Wondratschek, *Bilbao Crystallographic Server. II. Representations of crystallographic point groups and space groups*, Acta Crystallogr. Sect. A **62**, 115 (2006).

[76] M. I. Aroyo, J. M. Perez-Mato, D. Orobengoa, E. Tasci, G. De La Flor, and A. Kirov, *Crystallography online: Bilbao crystallographic server*, Bulg. Chem. Commun. **43**, 183 (2011), https://www.bgcryst.com/symp10/proceeding/02_Aroyo_183-197.pdf.

[77] Samuel V. Gallego, Emre S. Tasci, Gemma de la Flor, J. Manuel Perez-Mato, and Mois I. Aroyo, *Magnetic symmetry in the Bilbao Crystallographic Server: A computer program to provide systematic absences of magnetic neutron diffraction*, J. Appl. Crystallogr. **45**, 1236 (2012).

[78] Nikhil Sivadas, Satoshi Okamoto, Xiaodong Xu, Craig. J. Fennie, and Di Xiao, *Stacking-dependent magnetism in bilayer* CrI_3, Nano Lett. **18**, 7658 (2018).

[79] Vijay Kumar Gudelli and Guang-Yu Guo, *Magnetism and magneto-optical effects in bulk and few-layer* CrI_3*: A theoretical* GGA + U *study*, New J. Phys. **21**, 053012 (2019).

[80] John P. Perdew, Kieron Burke, and Matthias Ernzerhof, *Generalized gradient approximation made simple*, Phys. Rev. Lett. **77**, 3865 (1996).

[81] Sándor Tóth, Björn Wehinger, Katharina Rolfs, Turan Birol, Uwe Stuhr, Hiroshi Takatsu, Kenta Kimura, Tsuyoshi Kimura, Henrik M Rønnow, and Christian Rüegg,

Electromagnon dispersion probed by inelastic x-ray scattering in $LiCrO_2$, Nat. Commun. **7**, 13547 (2016).

[82] P. Padmanabhan, F. L. Buessen, R. Tutchton, K. W. C. Kwock, S. Gilinsky, M. C. Lee, M. A. McGuire, S. R. Singamaneni, D. A. Yarotski, A. Paramekanti, J. X. Zhu, and R. P. Prasankumar, *Coherent helicity-dependent spin-phonon oscillations in the ferromagnetic van der Waals crystal* CrI_3, Nat. Commun. **13**, 4473 (2022).

[83] Igor Mazin (The PRX Editors), *Editorial: Altermagnetism—a new punch line of fundamental magnetism*, Phys. Rev. X **12**, 040002 (2022).

[84] Libor Šmejkal, Jairo Sinova, and Tomas Jungwirth, *Emerging research landscape of altermagnetism*, Phys. Rev. X **12**, 040501 (2022).

[85] Giuseppe Grosso and Giuseppe Pastori Parravicini, *Solid State Physics* (Academic Press, New York, 2013).